Probing the regular nature of the spacetime by direct measurement of black hole properties

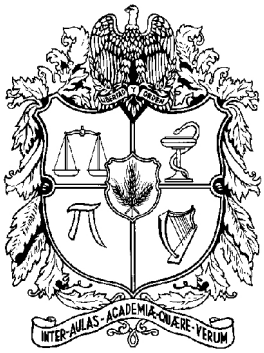

UNIVERSIDAD
NACIONAL
DE COLOMBIA

Alejandro Cárdenas Avendaño

Observatorio Astronómico Nacional de Colombia

Advisor: Prof. Alexis Larrañaga

A thesis submitted for the degree of

Master of Science in Astronomy

Bogotá D.C. 2015

Página de Aceptación

_____
_____
_____
_____
_____
_____

_____
Prof. Leonardo Castañeda
Universidad Nacional de Colombia
Bogotá D.C, Colombia
Jurado/Referee

_____
Prof. Cosimo Bambi
Fudan University
Shanghai, China
Jurado/Referee

_____
Prof. Alexis Larrañaga
Universidad Nacional de Colombia
Bogotá D.C, Colombia
Director/Advisor

Septiembre de 2015
Bogotá, D.C.
Colombia

Acknowledgements

I am grateful for the love and support of my family. My parents, Bertha Lucía and Alfredo, deserve special thanks for their endless support, generosity and cheerfulness. It would be impossible to acknowledge everything they have done to contribute. I also express my gratitude to María Alejandra, my standard basis, whose contribution to my life is also immeasurable, for her huge patience and love.

Thanks are due to my advisor, Dr. Alexis Larrañaga, for the seed ideas. Profound thanks are due to Dr. Olivier Sarbach, Dr. Luis Lehner and Dr. Cosimo Bambi for patience and guidance through the late stages of this project, which have broadened my knowledge of physics in general. I am particularly indebted to Prof. Benjamín Calvo-Mozo for his continued support, encouragement and good humor. Thanks are also due to Dr. Frédéric Vincent for a tremendously helpful correspondence concerning the use and modification of GYOTO, without his help, that part of my project would still be in its infancy stage. I would also like to express my gratitude to my thesis committee, for reviewing my thesis, for their comments and suggestions, and to the secretariat of the Observatory, Islena Bonilla, for administrative assistance and patience.

Great thanks are due to my fellow postgraduates Juan Camilo López-Carreño, Sebastián Castellanos-Durán and Jonah Miller, and to my dear friend Alexander Arredondo, for have helped me with the practicalities of my research, for their friendship and for providing such a supportive environment.

A Faculty of Sciences studentship from my University and a junior research position at the Konrad Lorenz Fundación Universitaria made it possible for me to work full-time on this thesis. Finally, thanks are due to the Perimeter Institute for Theoretical Physics, where part of this work was done, for their hospitality. Research at Perimeter Institute is supported by the Government of Canada through Industry Canada and by the Province of Ontario through the Ministry of Research and Innovation.

Abstract

In the following years Very Long Baseline Interferometry (VLBI) facilities will be able to directly image the accretion flow around the supermassive black hole candidate at the center of the Milky Way, Sgr A*. They will also be able to observe its shadow: an optical property which appears as a consequence of the strong gravitational field around it and which thus depends only on the physical parameters of the black hole. While there is no definitive evidence of the nature of the spacetime geometry around Sgr A*, it has been usually modeled by a Kerr black hole, by virtue of the no-hair theorem, which asserts that *all* uncharged black holes in 4-dimensional general relativity are described by this metric and thus completely specified by two parameters, the mass M and the spin parameter a. As a consequence, testing the no-hair theorem in nature with future observations allows us to not only verify that black holes in our universe are Kerr black holes, but to test the strong field predictions of general relativity

In this work I investigate if the shadow, image and spectrum of a non-Kerr regular black hole inspired by noncommutative geometry may provide a measurement of the parameters characterizing Kerr and non-Kerr regular black holes to distinguish one from the other. Specifically, the non-Kerr solution studied here is the rotating black hole found by Smailagic and Spallucci in 2010 and known as the "Kerrr" black hole, where the third "r" stands for regular, in the sense of a pathology-free rotating black hole. The general strategy to derive this generalized solution consists of prescribing an improved form of the energy-momentum tensor, which accounts, at least phenomenologically, for the noncommutative fluctuations of the manifold at the origin and which vanishes for large distances with respect to the noncommutative geometry scale, l_0.

The image and spectrum of Sgr A*, as the case of study, was modeled using the relativistic ray-tracing code GYOTO, assuming an optically thin, constant angular momentum torus in hydrodynamic equilibrium around the Kerr and "Kerrr" geometries. The model used includes a toroidal magnetic field and radiative cooling by bremsstrahlung, synchrotron, and inverse Compton processes. The assumptions provided here, for drawing the shadow and to model the accretion disk, do not provide a realistic scenario, but an easily accessible yet powerful analytical analogy.

Then comparisons with the Kerr geometry are calculated by using the observables defined by Hioki and Maeda and the distortion parameter

introduced by Tsukamoto, Li and Bambi. This work confirms that it is definitely challenging to test this kind of regular metric solely from observations of the shadow or accretion structures in the near future.

Keywords: Black hole physics, Accretion Disks, Noncommutative geometries

Resumen

En los próximos años las estaciones de interferometría de base ancha, Very Long Baseline Interferometry (VLBI), serán capaces de obtener imágenes de la acreción alrededor del candidato a agujero negro supermasivo en el centro de la Vía Láctea, Sag A*. Los resultados de estas campañas de observación permitirán observar también su sombra: un propiedad óptica que se genera como consecuencia del fuerte campo gravitacional alrededor del agujero negro y que depende solamente de los parámetros físicos del agujero negro.

Actualmente no hay evidencia definitiva sobre la naturaleza del espacio-tiempo alrededor de Sgr A* y usualmente ha sido modelado como un agujero negro de Kerr en virtud de los teoremas del no pelo, los cuales afirman que todos los agujeros negros sin carga, en cuatro dimensiones descritos por la relatividad general, dependen únicamente de los dos parámetros de esa métrica; la masa y el parámetro de rotación. Por tal razón, probar la validez de este teorema en la naturaleza a través de observaciones nos permitirá, no solamente verificar si los agujeros negros del Universo están descritos por la métrica de Kerr, sino además probar las predicciones de la relatividad general en el campo fuerte.

En este trabajo investigo si la sombra, imagen y espectro de un agujero negro regular diferente de Kerr, inspirado de la geometría no conmutativa, permite medir los parámetros que caracterizan los agujeros negros y distinguir sus diferencias. Específicamente, la solución estudiada acá es la rotante encontrada por Smailagic y Spallucci en 2010 conocida como el agujero negro de "Kerrr", en donde la tercera "r" simboliza la naturaleza regular de esa solución. La forma general de obtener ese tipo de soluciones consiste en modificar el tensor de momento y energía de tal manera que codifique, al menos de forma fenomenológica, las fluctuaciones no conmutativas de la variedad en el origen y que desaparecen a grandes distancias, con respecto a la escala de la geometría no conmutativa. La imagen y el espectro de Sgr A*, como caso de estudio, fueron modeladas usando el código de trazado de rayos GYOTO, asumiendo un toro ópticamente delgado con momento angular constante en equilibrio hidrodinámico, alrededor de las geometrías de Kerr y "Kerrr". El modelo usado incluye un campo magnético toroidal y enfriamientos radiativos por bremsstrahlung, synchroton y procesos de Compton inverso. Las simplificaciones hechas acá, para dibujar la sombre y modelar el disco de acreción, no representan un escenario real, pero son buenas analogías analíticas.

Las comparaciones son hechas a través de los observables definidos por Hioki y Maeda y el parámetro de distorsión de Tsukamoto, Li y Bambi. Este trabajo confirma la complejidad y dificultad de probar este tipo de soluciones a través de únicamente mediciones de la sombra y estructura de acreción en el futuro próximo.

Palabras clave: Física de agujeros Negros, Discos de Acreción, Geometrías no conmutativas

Contents

List of Figures

Chapter 1

Introduction

Black holes are fascinating objects because they challenge our understanding of many fundamental physical processes. In words of Chandrasekhar: *"The black holes of nature are the most perfect macroscopic objects there are in the universe: the only element in their construction are our concepts of space and time. And since the general theory of relativity provides only a single unique family of solutions for their descriptions, they are the simplest objects as well"* [29]. One can understand the latter *perfection* and *simplicity* by virtue of one of the most important theorems of general relativity; the so-called "No hair theorem" [26, 85], which states that all stationary black holes are the same up to two parameters, i.e., the mass, M, and the spin angular momentum, J, of the black hole. Thus, from an outside observer perspective, once they form and settle down to the stationary configuration, they can be described *exactly,* without any approximation in any single equation, representing an unique situation in physics and, in that sense, a *perfect* object.

The image shown in Fig. 1.1 is, to my understanding, the best simulated-image we have of the appearance of a black hole seen by a "near" observer. It has many relativistic effects, e.g., bending of light rays, luminosity and redshift effects and a fully relativistic accretion disk. It was produced by a code written in C++ (40.000 lines) and took several hours running on a ten-core E5-2680 Intel Xeon CPUs with 156 GB RAM [54].

The foundation of that simulated-image is the Kerr metric, written in Boyer-Lindquist coordinates, and honors perfectly the pioneering work of Bardeen [17], where he studied, for the first time, the gravitational lensing by spinning black holes. Despite of this seminal work, gravitational lensing by black holes remained quiet until decades later, when the prospect for actual observations brought it to the fore [54].

Nevertheless, the nature of black holes is far for being clear: there is no evidence that the spacetime geometry around Sagittarius A* (Sgr A*), M87 or any other black hole candidate is really described by the Kerr metric[1], but for the first time Very Long Baseline Interferometry (VLBI) facilities will be able to directly observe the so-called

[1]There is no alternative explanation in the framework of conventional physics. For instance, stellar mass black hole candidates are too heavy to be neutron stars [59, 10] and the exact physical mechanisms of the supermassive black holes, like Sgr A*, origin and early growth are still not firmly established [32].

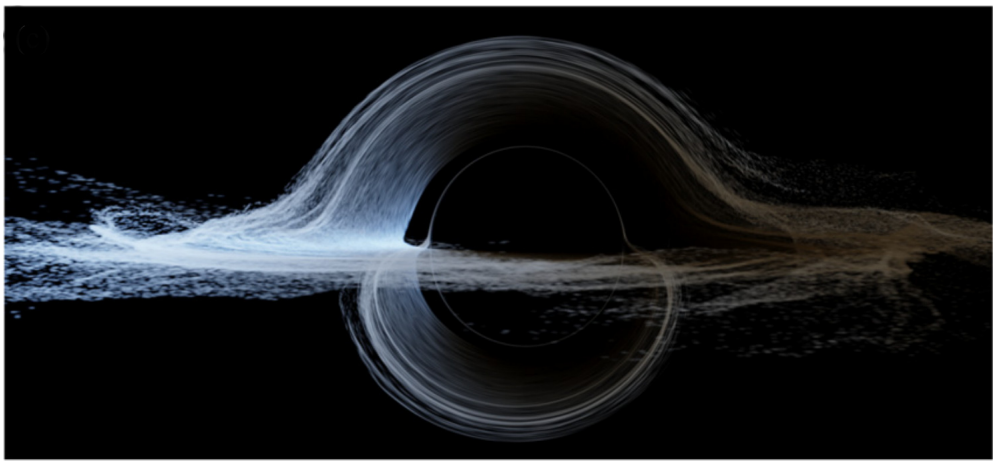

Figure 1.1: Figure from *Gravitational lensing by spinning black holes in astrophysics, and in the movie Interstellar*, O. James et al., Class. Quantum Grav. **32** (2015) 065001 [54]. This image is what a fully realistic accretion disk would truly look like to an observer near the black hole, i.e., $r_c = 74.1\,M$ and $\theta_c = 86.56$. The inner and outer radii are located at $r = 9.26\,M$ and $r = 18.70\,M$ before placed around the black hole.

black hole shadow, an optical property which appears as a consequence of the strong gravitational field around the black hole, and image the accretion flow around the supermassive black hole candidates, particularly one at the center of the Milky Way, Sgr A*, and M87 [34, 33, 42, 47, 48], giving us an unique opportunity to test the Kerr or non-Kerr nature of astrophysical black holes. However, it is important to stress that in order to really test the nature of the compact object, at least two independent measurements are necessary [11].

Different authors have proposed different ways to test the geometry around black hole candidates (see, for instance, Ref. [82] and references therein for tests with observations in the electromagnetic spectrum, Ref. [104] and references therein for tests based on strong gravity and gravitational waves, and for a general review Ref. [9]). If astrophysical black holes are not described only by the mass and the spin, the only two independent multipole moments of the Kerr black hole [50], it is expected that the deviations from the Kerr metric are manifestly predominant in the immediate vicinity of black holes [58]. If one parametrize a potential deviation from the Kerr metric in terms of a parameter, or a family of parameters, if a measurement yields a nonzero deviation of that parameter and if it is otherwise known to be a black hole, i.e. to have a horizon[2], then the compact object cannot be a Kerr black hole and then the deviation from Kerr metric implies that both the no-hair theorem and general relativity are violated.

Since I want to test the Kerr metric, I consider a background more general than the Kerr solution and that includes the Kerr solution as special case, proposed by

[2]The event horizon is the defining characteristic of a black hole and, to date, observational evidence for the presence of an *apparent* and *trapping* horizons, which are defined using local measurements, in astrophysical black holes exists [84, 34, 19, 98].

Smailagic and Spallucci in Ref. [89]. It is a regular, i.e., *pathology-free*, rotating black hole by choosing a non-commutative geometry inspired matter source as the input of the Einstein equations, based on the seminal work presented in Ref. [77] where a minimal length l_0 was introduced which takes into account the noncommutativity of spacetime, determining the fundamental discretization of it. From the fundamental view of noncommutative geometry, the idea of spacetime as a manifold of points breaks down at Planck scale and the parameter introduced in that solutions cannot be observed at presently accessible energies, i.e., $l_0 < 10^{16}\, cm$ [77]. However, it has been shown recently that this parameter affects the shape of the black hole shadow [24, 100], offering a way to probe and determine not only the spacetime noncommutative parameter but also as a test of general relativity via astronomical instruments in the near future.

In this work I am going to study the shadow, image and spectra of an accretion structure around Sgr A* (modeled as an optical thin, constant angular momentum ion torus in hydrodynamic equilibrium proposed in Ref. [91]) produced by assuming Kerr and the non-Kerr regular geometry proposed by Smailagic and Spallucci in Ref. [89] as the background. Then using the observables defined in Refs. [51, 93] I will compare these solutions.

This work is organized as follows. In chapters 2 and 3 I introduce the metrics that will be used in the rest of the work. In chapter 4 I review the concept and the calculation of the black hole shadow. Chapter 5 is devoted to the relativistic ray tracing and the implementation of the disk accretion by using GYOTO [96, 91]. The observables and comparisons are shown in chapter 6. Results, summary and conclusions are presented in chapter 7. Throughout this work geometrized units[3] are used unless otherwise mentioned.

[3]In this units, $G = c = 1$, meaning that mass, distance and energy have the same units, i.e., $[L]$. The SI units can always be recovered by adding c and G properly, e.g., $t \to ct$ and $M \to GM/c^2$.

Chapter 2

The Kerr Geometry

Among the several black hole solutions of the Einstein's equations, the Kerr geometry [60] is without any doubts the most appropriate to fit the observational data[1], showing that collapsed objects exhibit angular momenta [15] . In this chapter I will study the formulae of the Kerr metric for its photon orbits.

2.1 Kerr spacetime in Boyer-Lindquist coordinates

The spacetime of a rotating black hole is well described by the Kerr metric in Boyer-Lindquist coordinates [18]

$$\begin{aligned} ds^2 &= -\left(1-\frac{2Mr}{\rho^2}\right)dt^2+\frac{\rho^2}{\Delta}dr^2+\rho^2 d\theta^2 \\ &\quad -\frac{4Mra\sin^2\theta}{\rho^2}dtd\phi+\frac{A\sin^2\theta}{\rho^2}d\phi^2, \end{aligned} \tag{2.1}$$

where

$$\Delta(r) \coloneqq r^2-2Mr+a^2 \tag{2.2}$$

$$\rho^2(r,\theta) \coloneqq r^2+a^2\cos^2\theta \tag{2.3}$$

$$A(r,\theta) \coloneqq \left(r^2+a^2\right)^2-\Delta a^2\sin^2\theta. \tag{2.4}$$

The parameters M and a represent the mass and the spin angular momentum parameter of the black hole, respectively[2]. The covariant and the contravariant forms

[1] Initial deviations from the Kerr spacetime, according to 4-dimensional general relativity, would be radiated away through the emission of gravitational waves [81]. On the other hand, any initial electric charge would be quickly neutralized due to the presence of a highly ionized host environment [13].

[2] Note that the angular momentum is specified in terms of the dimensionless spin parameter $a = Jc/GM^2$, where J is the angular momentum and the cosmic censorship hypothesis ensures that $|a| \leq 1$. For gravitational processes, the mass acts as a scaling factor for distances, timescales, and energies [39].

of the foregoing metric are [17]:

$$(g_{ij}) = \begin{bmatrix} -\left(1-\frac{2Mr}{\rho^2}\right) & 0 & 0 & -\frac{4aMr\sin^2\theta}{\rho^2} \\ 0 & \frac{\rho^2}{\Delta} & 0 & 0 \\ 0 & 0 & \rho^2 & 0 \\ -\frac{4aMr\sin^2\theta}{\rho^2} & 0 & 0 & \left[r^2+a^2+\frac{2a^2Mr\sin^2\theta}{\rho^2}\right]\sin^2\theta \end{bmatrix} \tag{2.5}$$

$$\left(g^{ij}\right) = \begin{bmatrix} -\frac{A}{\rho^2\Delta} & 0 & 0 & -\frac{4aMr}{\rho^2\Delta} \\ 0 & \frac{\Delta}{\rho^2} & 0 & 0 \\ 0 & 0 & \frac{1}{\rho^2} & 0 \\ -\frac{4aMr}{\rho^2\Delta} & 0 & 0 & \frac{\left(\Delta-a^2\sin^2\theta\right)}{\rho^2\Delta\sin^2\theta} \end{bmatrix}. \tag{2.6}$$

The horizon[3] is a $2D$ surface of spherical topology, where the redshift factor vanishes

$$\Delta\left(r_{\pm}\right) = 0, \tag{2.7}$$

where the normal vector is null to surfaces $r = constant$ and satisfies

$$n_\alpha n_\beta g^{\alpha\beta} = g^{rr} = \frac{\Delta}{\rho^2} = 0,$$

which has in general two solutions. These are the outer horizon or event horizon

$$r_+ = M + \sqrt{M^2 - a^2}, \tag{2.8}$$

and the inner horizon or Cauchy horizon

$$r_- = M - \sqrt{M^2 - a^2}, \tag{2.9}$$

for all θ and ϕ. The gravitational redshift suppresses any emission at the event horizon. This results in the blackness of the black hole.

The hypersurfaces with $r = r_\pm$ are Killing horizons of the Killing vector field

$$\vec{\xi} = \vec{k} + \Omega_H \vec{m};\ \Omega_H = \frac{a}{r_\pm + a^2}, \tag{2.10}$$

where Ω_H is the angular velocity of the horizon (independent of the latitude).

At these surfaces we measure surface gravities

$$\kappa_\pm = \frac{r_\pm - r_\mp}{2\left(r_\pm^2 + a^2\right)}. \tag{2.11}$$

In the Kerr spacetime there is no globally static observer. Although k is time-like at infinity, it need not be time-like everywhere outside the horizon. For Kerr is found

[3]The inner root is very likely not important physically.

that

$$k^2 = g_{tt} = -\frac{\Delta - a^2 \sin^2\theta}{\varrho^2} = -\left(1 - \frac{2Mr}{r^2 + a^2\cos^2\theta}\right) \tag{2.12}$$

and k is therefore time-like, provided

$$r^2 + a^2\cos^2\theta - 2Mr > 0.$$

Now, for $M^2 > a^2$, this implies

$$r > r_E(\theta) = M + \sqrt{M^2 - a^2\cos^2\theta}. \tag{2.13}$$

The boundary of this region, $r = r_E(\theta)$, marks the transition of the coordinate t from a time-like to a space-like coordinate. This is called the static limit or ergosphere. The region $r_+ \leq r \leq r_E$ is the so-called ergoregion.

2.2 General orbits of particles (or photons)

The equations of motion of a test particle of mass μ are given by the general form of the Hamilton-Jacobi equation [25, 29]

$$\frac{\partial S}{\partial \lambda} = \frac{1}{2} g^{\alpha\beta} \frac{\partial S}{\partial x^\alpha} \frac{\partial S}{\partial x^\beta}, \tag{2.14}$$

where S is the Jacobi action.

Since the spacetime represented by (2.1) has two Killing vector fields, associated with the assumption of stationary and axisymmetric of the spacetime, there exists two conserved quantities for the general orbits of particles (or photons), i.e., the energy, E, and the axial component of the angular momentum, L_z, of the particle. Trivially the rest mass of the particle μ is also a constant ($\mu = 0$ for photons). However, these three constants just determine the motion when some restriction is imposed, which reduces the problem effectively to three or fewer dimensions, implying that a fourth constant of motion is needed in order to analyze the general case [25].

Given the lack of any obvious symmetry in r and θ in the metric (2.1), there was no reason to expect the geodesic to be completely integrable, so it came as a complete surprise when in 1968 Carter [25] showed that a fourth constant could be found because the Hamilton-Jacobi equation for the geodesics was separable[4] in r and θ [92].

Carter found the fourth constant by solving explicitly the Hamilton-Jacobi Eqn. (2.14) by assuming a Jacobi action of the form

$$S = \frac{1}{2}\mu^2\lambda - Et + L_z\phi + S_r(r) + S_\theta(\theta), \tag{2.15}$$

[4]The separability was not properly justified in Carter's seminal work [25], but it was well established in 1970 by Walker and Penrose where they showed that this separability follows from the existence of a Killing tensor [99].

where λ is an affine parameter[5] and S_r and S_θ are functions of only r and θ, respectively, and getting

$$\begin{aligned}\rho^2\mu^2 &= \frac{AE^2}{\Delta} - \left(\frac{\Delta - a^2\sin^2\theta}{\Delta\sin^2\theta}\right)L_z^2 - \frac{4aMrEL_z}{\Delta} \\ &\quad -\Delta\left(\frac{dS_r}{dr}\right)^2 - \left(\frac{dS_\theta}{d\theta}\right)^2,\end{aligned}$$

which can be factorized conveniently as

$$\begin{aligned}\rho^2\mu^2 &= \frac{1}{\Delta}\left[\left(r^2+a^2\right)E - aL_z\right]^2 - \frac{1}{\sin^2\theta}\left[L_z - aE\sin^2\theta\right]^2 - \\ &\quad -\Delta\left(\frac{dS_r}{dr}\right)^2 - \left(\frac{dS_\theta}{d\theta}\right)^2.\end{aligned}$$

The latter expression can be separated by introducing a constant, $\mathcal{K}$, such that

$$\begin{aligned}-\mathcal{K} &= r^2\mu^2 - \frac{1}{\Delta}\left[\left(r^2+a^2\right)E - aL_z\right]^2 + \Delta\left(\frac{dS_r}{dr}\right)^2 \\ \mathcal{K} &= \mu^2a^2\cos^2\theta + \frac{1}{\sin^2\theta}\left[L_z - aE\sin^2\theta\right]^2 + \left(\frac{dS_\theta}{d\theta}\right)^2.\end{aligned}$$

Hence, the Hamilton-Jacobi equation is separable in all four coordinates, making geodesic motion integrable and the Carter's constant is given by the relation

$$\mathcal{Q} = \mathcal{K} - \left(L_z - aE\right)^2. \tag{2.16}$$

Then, the formal solution for the Jacobi action is given by the integrals

$$\begin{aligned}S_r(r) &= \pm\int dr\frac{1}{\Delta}\sqrt{V_r} \\ S_\theta(\theta) &= \pm\int d\theta\sqrt{V_\theta},\end{aligned}$$

where

$$V_r = \left[\left(r^2+a^2\right)E - aL_z\right]^2 - \Delta\left[\mu^2r^2 + \left(L_z - aE\right)^2 + \mathcal{Q}\right] \tag{2.17}$$

and

[5]The parameter λ is related to the particle's proper time by $\lambda = \tau/\mu$ and is an affine parameter in the case when $\mu \to 0$

$$
\begin{aligned}
V_\theta &= \mathcal{Q} + (L_z - aE)^2 - \mu^2 a^2 \cos^2\theta \\
&\quad -\frac{1}{\sin^2\theta}\left(L_z - aE\sin^2\theta\right)^2 . \qquad (2.18)
\end{aligned}
$$

The quantities V_r and V_θ can be seen as effective potentials governing the particle motions in r and θ. The integrated forms of the geodesic and orbit equations can be obtained by using the fact that the partial derivatives of Jacobi function with respect to the constants of motion are themselves constants. Thus by differentiating with respect to them, i.e., $\mathcal{K}$,μ, E and L_z, the following expressions are derived, respectively,

$$
\begin{aligned}
\int \frac{dr}{\sqrt{V_r}} &= \int \frac{d\theta}{\sqrt{V_\theta}}, \\
\lambda &= \int \frac{r^2}{\sqrt{V_r}} dr + \int \frac{a^2\cos^2\theta}{\sqrt{V_\theta}} d\theta, \\
t &= \int \frac{a\Delta\left(L_z - aE\right) + \left[\left(r^2+a^2\right)E - aL_z\right]\left(r^2+a^2\right)}{\Delta\sqrt{V_r}} dr \\
&\quad + \int \frac{a\left(aE - L_z\right) + a\left[L_z - aE\sin^2\vartheta\right]}{\sqrt{V_\theta}} d\theta, \\
\phi &= \int \frac{a\Delta\left(L_z - aE\right) + a\left[\left(r^2+a^2\right)E - aL_z\right]}{\Delta\sqrt{V_r}} dr \\
&\quad + \int \frac{\left(aE - L_z\right) + \csc^2\theta\left[L_z - aE\sin^2\theta\right]}{\sqrt{V_\theta}} d\theta .
\end{aligned}
$$

The particle's 4-momentum is given by the expression

$$
p^\alpha = \mu \frac{dx^\alpha}{d\tau}
$$

and hence, from the partial derivatives of the Jacobi function with respect to the proper time and with respect to the coordinates, the relations between the momentum components and the constants of motion result

$$
\begin{aligned}
\mu E &= -p_t, \qquad (2.19) \\
\mu L_z &= p_\phi, \qquad (2.20) \\
\mathcal{Q} &= p_\theta^2 - (L_z - aE)^2 + \mu^2 a^2 \cos^2\theta \\
&\quad + \frac{1}{\sin^2\theta}\left(L_z - aE\sin^2\theta\right)^2 . \qquad (2.21)
\end{aligned}
$$

The above information is more conveniently expressed in terms of the first-order differential system:

$$\rho^2 \frac{dt}{d\tau} = -a\left[aE\sin^2\theta - L_z\right] + \frac{\left(r^2+a^2\right)\left[\left(r^2+a^2\right)E - aL_z\right]}{\Delta} \tag{2.22}$$

$$\rho^2 \frac{dr}{d\tau} = \pm\sqrt{V_r} \tag{2.23}$$

$$\rho^2 \frac{d\theta}{d\tau} = \pm\sqrt{V_\theta} \tag{2.24}$$

$$\rho^2 \frac{d\phi}{d\tau} = -\left[aE - \frac{L_z}{\sin^2\theta}\right] + \frac{a\left[\left(r^2+a^2\right)E - aL_z\right]}{\Delta}. \tag{2.25}$$

By introducing conveniently two conserved parameters, ξ and η, by[6]

$$\xi = \frac{L_z}{E} \tag{2.26}$$

and

$$\eta = \frac{\mathcal{Q}}{E^2}, \tag{2.27}$$

the photon trajectories, i.e., $\mu = 0$, can be fully determined in terms of this two parameters and Eqns. (2.22-2.25) can be rewritten as [29]

$$\rho^2 \frac{dr}{d\lambda} = \pm\sqrt{\mathcal{R}}, \tag{2.28}$$

$$\rho^2 \frac{d\theta}{d\lambda} = \pm\sqrt{\Theta}, \tag{2.29}$$

$$\rho^2 \frac{d\phi}{d\lambda} = \frac{1}{\Delta}\left(2Mar + \xi\csc^2\theta\left(\rho^2 - 2Mr\right)\right) \tag{2.30}$$

$$\rho^2 \frac{dt}{d\lambda} = \frac{1}{\Delta}\left(A - 2Mra\xi\right), \tag{2.31}$$

where

$$\mathcal{R} := \left(r^2 + a^2 - a\xi\right)^2 - \Delta\mathcal{I}, \tag{2.32}$$

$$\Theta := \mathcal{I} - \left(a\sin\theta - \xi\csc\theta\right)^2 \tag{2.33}$$

with

$$\mathcal{I}\left(\xi,\eta\right) := \eta + \left(a-\xi\right)^2. \tag{2.34}$$

Note again that the quantities $\mathcal{R}$ and Θ can be seen also as effective potentials governing the particle motions in r and θ, in terms of the conserved parameters, Eqns. (2.26) and (2.27), which are directly related to the impact parameters which

[6]The parameter ξ is the angular momentum per unit mass.

describe the direction of the particle as seen by an observer at a large distance r_{obs} from the black hole along the polar angle θ_{obs}. By assuming the spacetime symmetries, the equations for the coordinate t and ϕ result irrelevant for the rest of this work.

Given the functional structure of Eqns. (2.28) and (2.29), Eqns. (2.32) and (2.33) must be positive. Particularly, for Θ the latter condition implies the condition that the conserved parameter defined above, ξ and η, satisfies the constraint $\mathcal{I} \geq 0$.

2.2.1 Circular orbits

A circular orbit at some radius r must satisfy

$$\frac{dr}{d\lambda} = 0,$$

which implies, according to Eqns. (2.23) and (2.28)

$$\mathcal{R}(r) = V_r = 0. \tag{2.35}$$

However, the latter condition could be satisfied instantaneously just for a particular time, or set of times. In order to find the circular orbit it must be satisfied at all times, implying also the following condition

$$\frac{d\mathcal{R}(r)}{dr} = \frac{dV_r}{dr} = 0. \tag{2.36}$$

The investigation of the motion of test particles in the spacetime (2.1) is thus reduced to the study of motion in the effective potential. In particular, for timelike circular orbits in the equatorial plane the effective potential (2.17) can be written as

$$V(r) = \left(1 - \left(\frac{E}{\mu}\right)^2\right) r^4 - 2Mr^3 + \left[a^2\left(1 - \left(\frac{E}{\mu}\right)^2\right) + \left(\frac{L}{\mu}\right)^2\right] r^2 - 2M\left(a\left(\frac{E}{\mu}\right) - \left(\frac{L}{\mu}\right)\right) r. \tag{2.37}$$

When conditions (2.35) and (2.36) are satisfy there are three possible behaviors [17]:

1. $V''(r) > 0$: The photon is on a *stable circular orbit*, constrained to remain exactly at that value of r.

2. $V''(r) < 0$: The photon straddles the boundary between two regions with $V(r) < 0$; if perturbed one way it falls into the horizon, if perturbed the other way it flies outward (and, after reaching the outermost zero of V) turns back inward. In this case, the particle is on an *unstable circular orbit*.

3. $V''(r) = 0$: This is the junction between the two cases: *the marginally stable circular orbit*.

By taking the derivative of Eqn. (2.37):

$$V'(r) = 4\left(1-\left(\frac{E}{\mu}\right)^2\right)r^3 - 6Mr^2 + 2\left[a^2\left(1-\left(\frac{E}{\mu}\right)^2\right)+\left(\frac{L}{\mu}\right)^2\right]r - 2M\left(a\left(\frac{E}{\mu}\right)-\left(\frac{L}{\mu}\right)\right) \tag{2.38}$$

and using conditions (2.35) and (2.36), the following two linear combinations can be written

$$0 = \frac{1}{r}\left(V'(r) - \frac{V(r)}{r}\right) = \left(3r^2+a^2\right)\left(1-\left(\frac{E}{\mu}\right)^2\right) - 4Mr + \left(\frac{L}{\mu}\right)^2 \tag{2.39}$$

$$0 = V'(r) - \frac{2V(r)}{r} = 2\left(1-\left(\frac{E}{\mu}\right)^2\right)r^3 - 2Mr^2 + 2M\left(a\left(\frac{E}{\mu}\right)-L\right)^2 \tag{2.40}$$

which can be written as a quadratic equation for $\left(\frac{E}{\mu}\right)^2$, by using (2.39) to eliminate $\left(\frac{L}{\mu}\right)$ from (2.40), with solution [29]

$$\frac{E}{\mu} = \mathcal{E} = \frac{1-\frac{2M}{r}\pm\frac{aM^{1/2}}{r^{3/2}}}{\sqrt{1-\frac{3M}{r}\pm\frac{2aM^{1/2}}{r^{3/2}}}} \tag{2.41}$$

$$\frac{L_z}{\mu} = \mathcal{L} = \frac{\pm\sqrt{\frac{M}{r}}\mp\frac{2M}{r}\pm\frac{a^2\sqrt{M}}{r^{3/2}}}{\sqrt{1-\frac{3M}{r}\pm\frac{2a\sqrt{M}}{r^{3/2}}}}, \tag{2.42}$$

where the upper signs are for direct orbits and the lower signs for retrograde orbits, i.e., co-rotaton with $\mathcal{L}>0$ or counter-rotating with $\mathcal{L}<0$, respectively.

2.2.1.1 General Orbits in terms of η and ξ

Now, assuming the definitions (2.26) and (2.27) conditions (2.35) and (2.36) can be solved simultaneously for η and ξ as follows[7]

$$\xi = \frac{1}{a(r-M)}\left[M\left(r^2-a^2\right)-r\Delta\right] \tag{2.43}$$

$$\eta = \frac{r^3}{a^2(r-M)^2}\left[4M\Delta - r(r-M)^2\right]. \tag{2.44}$$

2.2.2 The photon orbit

Circular orbits do not exist for all values of r. The denominators for Eqns. (2.41) and (2.42) are real only if

[7] The solution also is tedious (see Ref. [29] Chap. 7) and a more general case will be shown explicitly in Sec. 3.2

$$r^{\frac{3}{2}} - 3M\sqrt{r} \pm 2a\sqrt{M} \geq 0. \tag{2.45}$$

The limiting case i.e.,

$$r^{\frac{3}{2}} - 3M\sqrt{r} \pm 2a\sqrt{M} = 0, \tag{2.46}$$

gives an orbit with infinity energy, per unit rest mass, i.e., a *photon orbit.* This photon orbit is the innermost boundary of the circular orbits for particles and it occurs a the root of Eqn. (2.46),

$$r_{ph} \equiv 2M\left\{1 + \cos\left[\frac{2}{3}\cos^{-1}\left(\mp\frac{a}{M}\right)\right]\right\}. \tag{2.47}$$

2.2.3 The marginally bound orbit

Bound[8] circular orbits exists for

$$r > r_{mb},$$

where r_{mb} is the marginally bound circular orbit

$$r_{mb} = 2M \mp a + 2\sqrt{M\left(M \mp a\right)} \tag{2.48}$$

2.2.4 The marginally stable orbit

According to the studies of Wilkins in Ref. [103], even bound circular orbits are not all stable, since stability requires that $V''(r) \geq 0$, which yields to the condition

$$r \geq r_{ms},$$

where r_{ms} is the radius of the *marginally stable orbit,* also known as the *innermost stable circular orbit (ISCO), [17]*

$$\begin{aligned} r_{ms} &= M\left[3 + Z_2 \mp \sqrt{\left(3 - Z_1\right)\left(3 + Z_1 + 2Z_2\right)}\right] \\ Z_1 &\equiv 1 + \left(1 - \frac{a^2}{M^2}\right)^{\frac{1}{3}}\left[\left(1 + \frac{a}{M}\right)^{\frac{1}{3}} + \left(1 - \frac{a}{M}\right)^{\frac{1}{3}}\right] \\ Z_2 &\equiv \sqrt{\frac{3a^2}{M^2} + Z_1^2}. \end{aligned} \tag{2.49}$$

[8] A bound orbit means that the particle rages over a finite interval of radius, neither being captured by the black hole or escaping to infinity [103].

2.2.5 Special Cases

2.2.5.1 Schwarzschild solution ($a = 0$)

For $a = 0$ Eqns. (2.1), (2.2), (2.3) and (2.4) reduce to the Schwarzschild solution in curvature coordinates. In this case the orbits described above take the following values

$$r_{ph} = 3M, \tag{2.50}$$
$$r_{mb} = 4M, \tag{2.51}$$
$$r_{ms} = 6M. \tag{2.52}$$

2.2.5.2 Extreme-rotating solution ($a = M$)

For $a = M$ the orbits described above take the following value

$$r_{ph} = r_{mb} = r_{ms} = M, \tag{2.53}$$

i.e, coincident with the horizon. However, as it was pointed out in Ref. [17], this is just an appearance of the Boyer-Lindquist coordinates, because all the above orbits, in this case, are outside of the horizon and all are distinct, since all the values of proper radial distance smaller or equal to r_{ms} becomes singulary projected into the Boyer-Lindquist coordinate location at $r = M$.

Chapter 3

The "Kerrr" Geometry

> "*We must confess in all humility that, while number is a product of our mind alone, space has a reality beyond the mind whose rules we cannot completely prescribe*"
>
> Carl Friedrich Gauss, 1830

It has been shown that noncommutativity eliminates point-like structures in favor of smeared objects in flat spacetime (see Ref. [76] for a review). The effect of smearing is mathematically implemented a "substitution rule": position Dirac-delta function is replaced everywhere with a Gaussian distribution of minimal width l_0 [76]. The symmetries of string theory (T-duality, in particular) suggest that there is, in a sense, a minimal measurable length, but the issue is far from settled; it could be, in particular, that certain particle-like topological defects, known as $D0$ branes, could probe shorter lengths [3].

The so-called noncommutative black holes are a class of stationary, axisymmetric, asymptotically flat metrics that describe spinning regular black holes. However here the metric coefficients depend non only on the mass and spin of the black hole but as well as on a free parameter l_0, identified as the *characteristic length* scale of the Gaussian smeared mass distribution. This class of metrics includes the Kerr metric as the special case when $l_0 \to 0$ [77, 89].

3.1 The "Kerrr" spacetime

The spacetime of this generalized rotating black hole is described in Boyer-Lindquist like coordinates [89]:

$$\begin{aligned} ds^2 &= -\left(1-\frac{2RM(R)}{\rho^2}\right)dt^2+\frac{\rho^2}{\Delta}dR^2+\rho^2 d\theta^2 \\ &\quad -\frac{4M(R)Ra\sin^2\theta}{\rho^2}dtd\phi+\frac{A\sin^2\theta}{\rho^2}d\phi^2, \end{aligned} \tag{3.1}$$

where

$$\Delta(R) := R^2 - 2M(R)R + a^2 \tag{3.2}$$
$$\rho^2(R,\theta) := R^2 + a^2\cos^2\theta \tag{3.3}$$
$$A(R,\theta) := \left(R^2+a^2\right)^2 - \Delta a^2 \sin^2\theta \tag{3.4}$$

and

$$M(R) = \frac{M}{\Gamma\left(\frac{3}{2}\right)}\gamma\left(\frac{3}{2};\left(\frac{R}{2l_0}\right)^2\right). \tag{3.5}$$

Here, as in Chap. (2), the parameters M and a represent the mass and the spin angular momentum parameter of the black hole, respectively. See Appendix (A) for its derivation and a discussion about its origin.

3.1.1 Horizons

Horizons in (3.1) are real solutions of the equation $\Delta(R) = 0$, or

$$R_H^2 + a^2 - \frac{2MR_H}{\Gamma\left(\frac{3}{2}\right)}\gamma\left(\frac{3}{2};\left(\frac{R_H}{2l_0}\right)^2\right) = 0, \tag{3.6}$$

which cannot be solved explicitly for R_H. However, equation (3.6) can be solved for the mass parameter $M(R_H)$ as function of the horizon radius R_H to see that for different values of l_0 and a, the metric displays different horizon structures, i.e., two horizons, one horizon, and no horizon. In this work the horizonless state will not be considered. Thus, for fixed value of the noncommutative parameter l_0, the spin parameter is required to $0 \leq a \leq a_{max}$, where a_{max} is obtained by solving numerically $\Delta(R) = 0$ and $\frac{d\Delta(R)}{dR} = 0$. The parameter space is shown in Fig. (3.1).

3.2 General orbits of particles (or photons)

This spacetime has the same conserved quantities as the presented in the last chapter, and the same procedure can be done in order to get the geodesics, i.e., using the Hamilton-Jacobi equation to obtain the equations of motion for a particle and assume the separability and one gets Eqns. (2.22), (2.23), (2.24) and (2.25) with the mass Mreplaced by $m(r)$.

Nevertheless, the study of radial-motion of photons will differ as it will be shown. To find these trajectories it is necessary to solve simultaneously, again,

$$\mathcal{R} = 0,\ \frac{d\mathcal{R}}{dR} = 0, \tag{3.7}$$

using Eqns. (4.9), (4.8), (2.27) and (2.26) as follows,

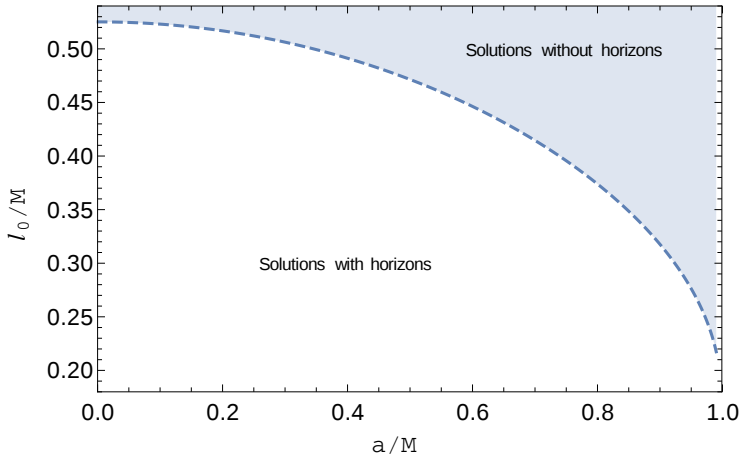

Figure 3.1: The parameter space describing the "Kerrr" black holes. The curve corresponds to the extremal configuration, characterized by having the maximum value of spin $a = a_{max}$ for a given l_0 and the presence of one degenerate horizon. Below this line, black holes have two horizons while configurations above the curve have no horizons. This figure can be compared with figure 1(b) of Ref. [100].

$$\mathcal{R} = R^4 + \left(a^2 - \xi^2 - \eta\right) R^2 + 2m\left[\eta + (a-\xi)^2\right] R - a^2\eta \tag{3.8}$$

$$\frac{d\mathcal{R}}{dR} = 4R^3 + 2\left(a^2 - \xi^2 - \eta\right) R + 2mf\left[\eta + (a-\xi)^2\right], \tag{3.9}$$

where

$$f \equiv 1 + \frac{m'(R)}{m(R)} r; \tag{3.10}$$

$$m'(R) = \frac{dm(R)}{dR} = \frac{2M}{\Gamma\left(\frac{3}{2}\right) l_0} \left(\frac{r}{l_0}\right)^2 e^{-\left(\frac{r}{l_0}\right)^2}. \tag{3.11}$$

Using conditions (3.7), multiplying Eqn. (3.9) by R and solving, one gets

$$\begin{aligned} 4R_{sph}^4 + 2\left(a^2 - \xi^2 - \eta\right) R_{sph}^2 + 2mR_{sph} f\left[\eta + (a-\xi)^2\right] &= 0 \\ 2mR_{sph}\left[\eta + (a-\xi)^2\right] &= -\frac{4R_{sph}^4}{f} - \frac{2\left(a^2 - \xi^2 - \eta\right) R_{sph}^2}{f} \end{aligned}$$

and replacing in Eqn. (3.8)

$$R_{sph}^4\left(1 - \frac{4}{f}\right) + \left(a^2 - \xi^2\right)\left(1 - \frac{2}{f}\right) R_{sph}^2 - \eta\left[a^2 + R_{sph}^2\left(1 - \frac{2}{f}\right)\right] = 0$$

or

$$\eta = \frac{R_{sph}^4 (f-4) + (a^2 - \xi^2)(f-2) R_{sph}^2}{f a^2 + R_{sph}^2 (f-2)}. \tag{3.12}$$

Replacing Eqn. (3.12) in Eqn. (3.9) and doing some algebra one gets a quadratic equation in ξ:

$$A\xi^2 + B\xi + C = 0,$$

where

$$\begin{aligned} A &\equiv a^2 (R_{sph} - mf) \\ B &\equiv -2am \left[(2-f) R_{sph}^2 - a^2 f\right] \\ C &\equiv -\left[R_{sph}^5 + R_{sph}^4 m (f-4) + 2R_{sph}^3 a^2 + 2R_{sph}^2 a^2 m (f-2) + R_{sph} a^4 + a^4 m f\right], \end{aligned}$$

its solution is

$$\xi = \frac{m\left[(2-f) R_{sph}^2 - a^2 f\right] - R_{sph}\left[R^2 - 2mR_{sph} + a^2\right]}{a (R_{sph} - mf)}. \tag{3.13}$$

The latter expression can be used to solve η from Eqn. (3.12)

$$\eta = \frac{R_{sph}^3 \left\{4ma^2 (2-f) - \left[R_{sph} - (4-f) m\right]^2\right\}}{a^2 (R_{sph} - mf)^2}. \tag{3.14}$$

The parameter R_{sph} is constrained by the existence conditions (2.33) and (2.34) with Eqns. (3.14) and (3.13), i.e.,

$$-R_{sph}^3 \left[R_{sph} \left\{\left(R_{sph}\left[1 + m'\right] - 3m\right)^2\right\} + 4a^2 \left\{rm' - m\right\}\right] \geq 0. \tag{3.15}$$

The condition for the orbit to be unstable is

$$\frac{d^2 V_{eff}}{dR^2} = 12R^2 + 4a(a-\xi) + 2\left[\eta + (a-\xi)^2\right]\left[2m' + rm'' - 1\right] < 0 \tag{3.16}$$

where

$$m''(R) = \frac{M e^{-\left(\frac{R}{2l_0}\right)^2}}{\Gamma\left(3/2\right)} \left(\frac{R}{2l_0^2}\right) \left[2 - \left(\frac{R}{2l_0}\right)^2\right]. \tag{3.17}$$

3.2.0.1 Generalized Schwarzschild solution ($a = 0$)

For $a = 0$ Eqns. (3.8) and (3.9) can be written as

$$\mathcal{R} = R^4 - \left(\xi^2 + \eta\right) R^2 + 2m\left[\eta + \xi^2\right] R - \eta \tag{3.18}$$

$$\frac{d\mathcal{R}}{dR} = 4R^3 - 2\left(\xi^2 + \eta\right) R + 2mf\left[\eta + \xi^2\right], \tag{3.19}$$

and imposing conditions (3.7) one gets

$$\eta = \frac{R^4\left[(f-4)\,m + R\right]}{fm - R} \tag{3.20}$$

$$\xi = -\sqrt{\frac{R^3\left[2 + (f-4)\,mR + R^2\right]}{R - fm}} \tag{3.21}$$

3.2.1 Circular orbits

The circular orbits calculated in Chap. (2) cannot be written in an exact form in this case, due to the non trivial functions involved, however in this section some general expression will be derived that allow suitable expression to get the results numerically.

Assuming that the particles are moving in circular geodesic orbits on the equatorial plane with four-velocity

$$\begin{aligned} u^\mu &= \left(u^t, 0, 0, u^\phi\right), \\ &= u^t\left(1, 0, 0, \Omega\right), \end{aligned} \tag{3.22}$$

where Ω is the coordinate angular velocity of the circular orbit, defined as

$$\begin{aligned} \Omega &\equiv \frac{u^\phi}{u^t} \\ &= -\frac{g_{t\phi} + \xi g_{tt}}{g_{\phi\phi} + \xi g_{t\phi}}, \end{aligned} \tag{3.23}$$

where the constants of motion (2.19) and (2.20) were written as

$$\mathcal{E} = -u^t\left(g_{tt} + \Omega g_{t\phi}\right) \tag{3.24}$$

$$\mathcal{L} = u^t\left(g_{t\phi} + \Omega g_{\phi\phi}\right) \tag{3.25}$$

and $g_{\mu\nu}$ are the metric coefficients obtained from Eqn. (3.1).

From the above definition one gets

$$\xi = -\frac{g_{t\phi} + \Omega g_{\phi\phi}}{g_{tt} + \Omega g_{t\phi}}. \tag{3.26}$$

Assuming the normalization relation

$$\begin{aligned} u_\mu u^\mu &= u_t u^t + u_\phi u^\phi \\ &= -1 \end{aligned} \tag{3.27}$$

is possible to solve for u_t, i.e. the particle's energy, in terms of Ω and the metric coefficients as follows. From Eqns. (3.24) and (3.25) one gets

$$u^t = \frac{u_t}{g_{tt} + \Omega g_{t\phi}} \tag{3.28}$$

and

$$u_\phi = u^t \left(g_{t\phi} + \Omega g_{\phi\phi} \right)$$

which combined give

$$u_\phi = u_t \frac{g_{t\phi} + \Omega g_{\phi\phi}}{g_{tt} + \Omega g_{t\phi}}. \tag{3.29}$$

From Eqn. (3.23) one obtains

$$u^\phi = \frac{\Omega u_t}{g_{tt} + \Omega g_{t\phi}}. \tag{3.30}$$

Plugging Eqns. (3.28), (3.29) and (3.30) in (3.27) finally the energy per unit mass is

$$u_t = -\mathcal{E} = -\frac{g_{tt} + \Omega g_{t\phi}}{\sqrt{-g_{tt} - 2g_{t\phi}\Omega - g_{\phi\phi}\Omega^2}}. \tag{3.31}$$

In a similar fashion, the other conserved quantity can be found

$$u_\phi = -\mathcal{L} = -\frac{g_{t\phi} + \Omega g_{\phi\phi}}{\sqrt{-g_{tt} - 2g_{t\phi}\Omega - g_{\phi\phi}\Omega^2}}. \tag{3.32}$$

The important circular orbits shown in Chap. (2), i.e. the photon orbit, Eqn. (2.47), the marginally bound orbit, Eqn. (2.48) and marginally stable orbit, Eqn. (2.49), can be obtained from Eqns. (3.31) and (3.32).

Fig. (3.2) shows the energy of the particle (Eqn. 3.31) around the black hole, Fig. (3.3) shows the angular velocity (Eqn. (3.23)) and Fig. (3.4) show the marginally stable orbit (ISCO) for orbits in the equatorial plane, i.e. $\theta = \pi/2$.

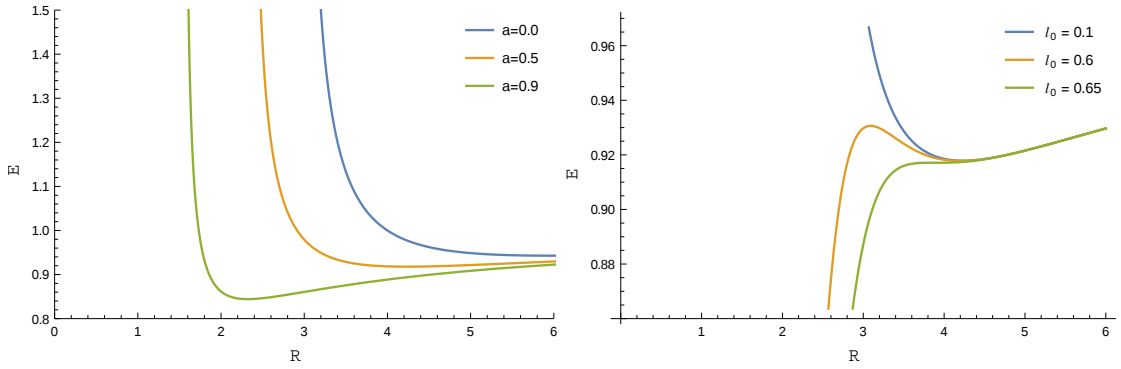

Figure 3.2: Energy of the particle in the equatorial plane for (*Left*) $l_0 = 0.0$ and different values of a and for (*Right*) $a = 0.5$ and different values of the noncommutative parameter l_0. In this plot $M = 1$ and the cases $l_0 = 0.6$ and $l_0 = 0.65$ are horizonless black holes.

By virtue of the regularity of the metric (3.1) the energy of the particle and the angular velocity Ω the do not diverge, see Figs. (3.2 and 3.3, *Left* panels). For the case of $l_0 = 0.1$ it gets a finite value. Note that the other two cases are plotted to better show the latter statement, however those are cases where there are no horizons, see Fig. (3.1). Note the bizarre behavior of orbits at small radii in the space-time when the solution considered is horizonless, i.e., $l_0 = 0.6$ and $l_0 = 0.65$, see Fig. (3.1).

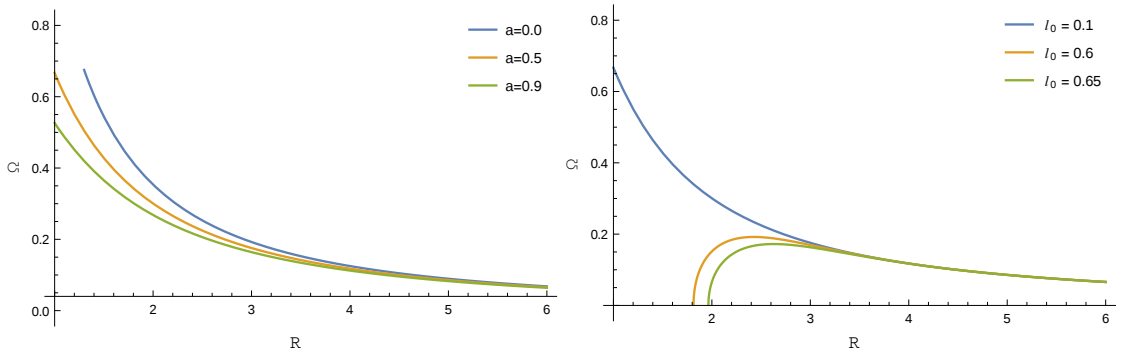

Figure 3.3: Angular velocity of the particle in the equatorial plane for (*Left*) $l_0 = 0.0$ and different values of a and for (*Right*) $a = 0.5$ and different values of the noncommutative parameter l_0. In this plot $M = 1$. The cases $l_0 = 0.6$ and $l_0 = 0.65$ are horizonless black holes. The (*Left*) panel can be compared with Fig. 8.10 of Ref. [22].

Finally, and for reasons that will be shown in Chap. (5), it is important to know where the ISCO is located for each geometry. However, as it can be seen from Fig. (3.4) the noncommutative parameter do not affect drastically its value, e.g. $r_{ISCO} = 5.99998$ for $l_0 = 0.65$ and $a/M = 0$, which means a difference of about 0.00207246% for the Schwarzschild case. However, for horizonless states the difference is drastically increased, e.g. $r_{ISCO} = 3.95201$ for $l_0 = 0.65$ and $a/M = 0.5$, which

means a difference of about 28.009% for the Kerr geometry. Note that the ISCO take values continuously over the whole range of a/M, but here I just showed some particular values, since the calculation is computationally expensive in the "Kerrr" geometry.

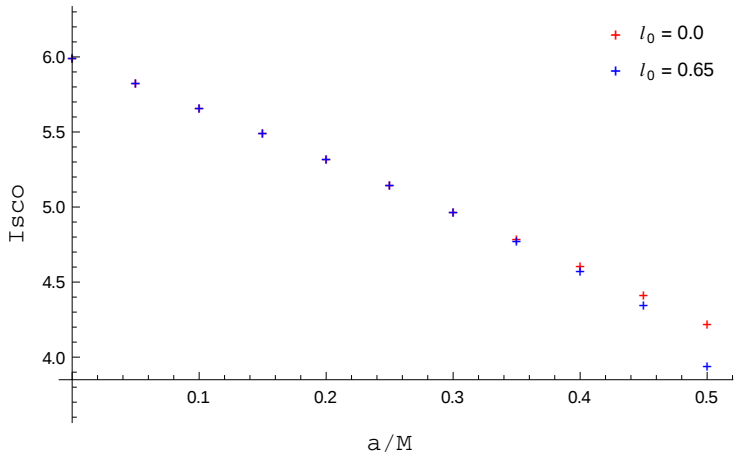

Figure 3.4: Value of the ISCO for $l_0 = 0.0$ (Kerr) and $l_0 = 0.65$ ("Kerrr" without horizons) at some values of a/M. For the Schwarzschild case, i.e. $l_0 = 0.0$ and $a/M = 0$ the value obtained is 6.0, Eqn. (2.52). The results for the Kerr case can be compared with Fig. 8.11 of Ref. [22].

Chapter 4

Black Hole Shadow

It is conceptually interesting, if not astrophysically very important, to calculate the precise apparent shape of a black hole [16]. But before analyzing the general problem of a black hole surrounded by an emitting accretion disk, it is interesting to investigate a more simple case in which the dynamics are already contained, namely the problem of the return of light from a bare black hole illuminated by a source of illumination whose angular size is large compared with the angular size of the black hole [65, 16].

To start, lets assume an observer located at infinity $r = \infty$ with the inclination angle i, which is defined by the angle between the rotation axis of the collapsed object and the observer's line of sight. The celestial coordinates (α, β) [95] of the observer are the apparent angular distances of the image on the celestial sphere measured from the direction of the line of sight and will be defined and derived in Sec. (4.1).

4.1 Celestial Coordinates [95]

Given the asymptotic properties of the metrics described in Chaps. (2) and (3), an observer far away from the black hole can set up a reference euclidean coordinate system (x, y, z) with the black hole at the origin (see Fig. 4.1) and rotating around the z axis. These euclidean coordinates will coincide with the Boyer-Lindquist coordinates (r, θ, ϕ) for $r \gg 1$.

If one assumes that the black hole rotates in the counterclockwise direction with respect to the positive z axis and, for simplicity and by virtue of the spherical symmetry, that the observer is located at $\phi_o = 0$, one can draw a better picture to work with, in which the y axis is contained within the $\alpha - \beta$ plane and the observer is contained within the $x - z$ plane (see Fig. 4.2).

The observer will be located at coordinates $(r_0, i, 0)$ and the source at coordinates (r_s, θ_s, ϕ_s). Thus, the image seen by the observer is a projection of the real system over the $\alpha - \beta$ plane, where α and β are the celestial coordinates; the plane is constructed so that the normal vector of the plane is parallel to the observer's line of sight as is shown in Fig. (4.1).

In the observer's reference frame, an incoming light ray is described by a parametric curve $X(r)$, $Y(r)$ and $Z(r)$, where r satisfies $r^2 = X^2(r) + Y^2(r) + Z^2(r)$.

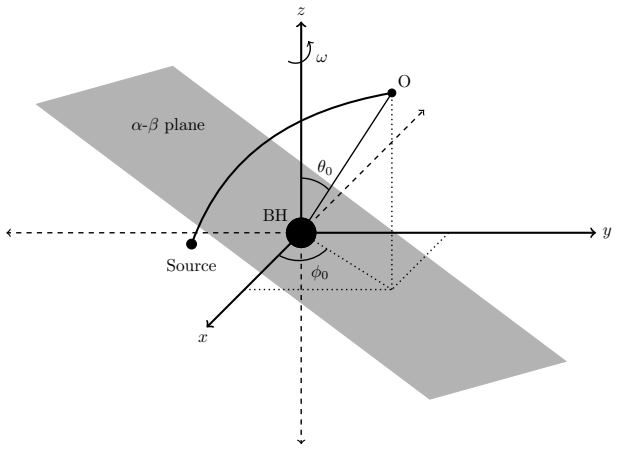

Figure 4.1: An observer far away from the astrophysical system is able to set up a curvilinear coordinate system, for convenience we take the Cartesian coordinates (x, y, z) with the black hole at the origin. The observer's position is given by (r_0, i, φ_0), with $r_0 \gg 1$. The coordinate system is constructed such that the z axis matches with the rotation axis of the black hole. Figure courtesy of D. Torres.

The tangent vector to this parametric curve at the observer's position is given by

$$\vec{\mu} = (\mu_1, \mu_2, \mu_3) = \left.\frac{dX}{dr}\right|_{r_0} + \left.\frac{dY}{dr}\right|_{r_0} + \left.\frac{dZ}{dr}\right|_{r_0}, \tag{4.1}$$

and describes the straight line which intersect the $\alpha - \beta$ plane at the point (α_i, β_i), which is described parametrically as

$$\frac{x - x_0}{\mu_1} = \frac{y - y_0}{\mu_2} = \frac{z - z_0}{\mu_3}, \tag{4.2}$$

where (x_0, y_0, z_0) represents the observer's position in Cartesian coordinates. By virtue of the symmetry, this point in spherical coordinates is written as $(r_0 \sin i, 0, r_0 \cos i)$ and the point (α_i, β_i) over the $\alpha - \beta$ in terms of the celestial coordinates is given by $(x_i, y_i, z_i) = (-\beta_i \cos i, \alpha_i, \beta_i \sin i)$, as seen from Fig. (4.2). In order to find the celestial coordinates, the points (x_0, y_0, z_0) and (x_i, y_i, z_i) are replaced in Eqn. (4.2) and one gets

$$\frac{-\beta_i \cos i - r_0 \sin i}{\mu_1} = \frac{\alpha_i}{\mu_2} = \frac{\beta_1 \sin i - r_0 \cos i}{\mu_3}. \tag{4.3}$$

To find the celestial coordinates, the tangent vector $\vec{\mu}$ must be written in spherical coordinates. Using the Eqn. (4.1) and evaluating on the observer's position the coefficients of $\vec{\mu}$ take the form

$$\mu_1 = \sin i + r_0 \cos i \left.\frac{d\theta}{dr}\right|_{r_0}, \tag{4.4}$$

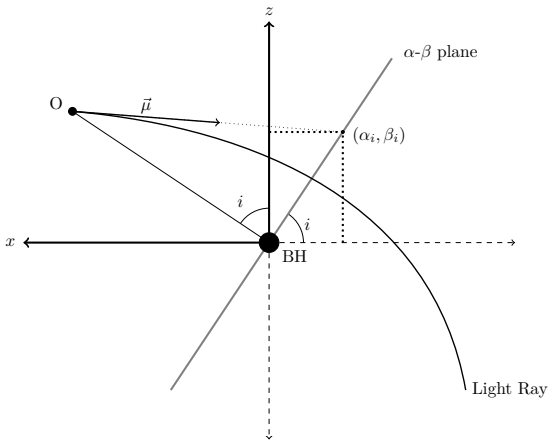

Figure 4.2: Simplified description of the system, where i represents the angle between the observer's line of sight and the rotation axis of the BH. The α-β plane is constructed such that it is perpendicular to the line segment $\overline{OBH}$, and the points (α_i, β_i) represent the projection of the real system over the α-β plane seen by the observer. The vector $\vec{\mu}$ represents the tangent vector to the ray light curve at observer's position. Figure courtesy of D. Torres.

$$\mu_2 = r_0 \sin i \left.\frac{d\phi}{dr}\right|_{r_0}, \tag{4.5}$$

$$\mu_3 = \cos i - r_0 \sin i \left.\frac{d\theta}{dr}\right|_{r_0}, \tag{4.6}$$

these three expressions allow to write Eqn. (4.3) as

$$\frac{-\beta_i \cos i - r_0 \sin i}{\sin i + r_0 \cos i \left.\frac{d\theta}{dr}\right|_{r_0}} = \frac{\alpha_i}{r_0 \sin i \left.\frac{d\phi}{dr}\right|_{r_0}} = \frac{\beta_1 \sin i - r_0 \cos i}{\cos i - r_0 \sin i \left.\frac{d\theta}{dr}\right|_{r_0}}. \tag{4.7}$$

Finding the celestial coordinates reduces to solve equation Eqn. (4.7) for α_i and β_i with r_0 at infinite. Solving for β_i one gets

$$\beta_i = \lim_{r_0 \to \infty} r_0^2 \left.\frac{d\theta}{dr}\right|_{r_0}, \tag{4.8}$$

and solving for α_i

$$\alpha_i = \lim_{r_0 \to \infty} -r_0^2 \sin\theta_0 \left.\frac{d\phi}{dr}\right|_{r_0}. \tag{4.9}$$

Using Eqns. (2.28), (2.29) and (2.30) and taking the limit, the celestial coordinates can be written as

$$\beta_i = \sqrt{\eta + a^2 \cos^2 i - \xi^2 \cot^2 i}, \tag{4.10}$$
$$\alpha_i = -\xi \csc i. \tag{4.11}$$

4.2 Black Hole Shadow

As seen by a distant observer, a black hole will appear as a *"black hole"* in the middle of the larger bright source. The rim of the "black hole" corresponds to photon trajectories which are marginally trapped by the black hole; they spiral around many times before they reach the observer [65, 40, 63].

Every orbit can be characterized by the constants of motion ξ and η, and the set of unstable circular orbits (ξ_c, η_c) can be used to plot a closed curve in the $\alpha\beta$ plane which represents the boundary of the black hole shadow using, Eqns.(4.10), (4.11), (3.14) and (3.13), and considering the light rays emitted at infinity, which will be either captured by the black hole or scattered back to infinity, see Figs. (4.3), (4.4) and (4.5). The condition to have unstable orbits, i.e., Eqn. (3.15), has to be checked numerically, since there is no a sufficient condition for the existence of a circular orbit. Note that the boundary of the shadow depends only on the geometry of the background.

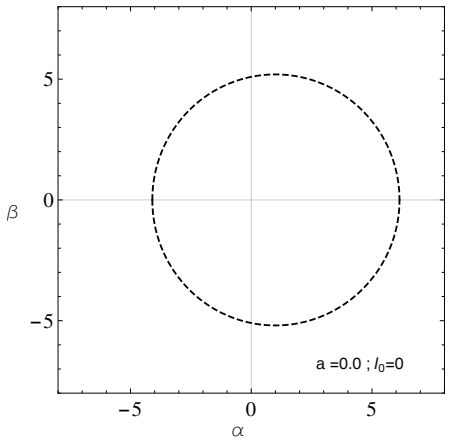

Figure 4.3: Shadow of the Schwarzschild black hole. The celestial coordinates (α, β) are measured in the unit of the black hole mass M and $i = \pi/2$.

If the rotation parameter a is zero (as is shown in Fig. (4.3)), the shape is a circle, while if it rotates (as is shown Figs. (4.4) and (4.5)), the shape is distorted. In Figs. (4.4) and (4.5) the shadows of the Kerr black holes are shown in black while the shadow of the Kerrr black holes are shown in green. The inside of this distorted silhouette is the region where null-geodesics are captured by the event horizon. The typical feature is that the left-hand side of the disk is chipped away [51, 93].

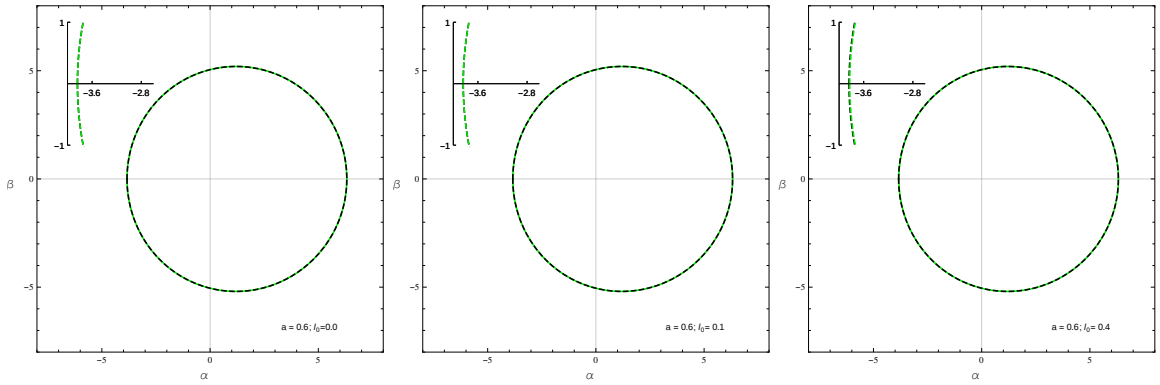

Figure 4.4: Shadows of the Kerr and "Kerrr" black holes for various values of the noncommutative parameter l_0. The celestial coordinates (α, β) are measured in the unit of the black hole mass M and $i = \pi/2$ for all figures. The shadows of the Kerr black holes are shown in black while the shadow of the "Kerrr" black holes are shown in green. This figures can be compared with Fig. 4 of Ref. [100].

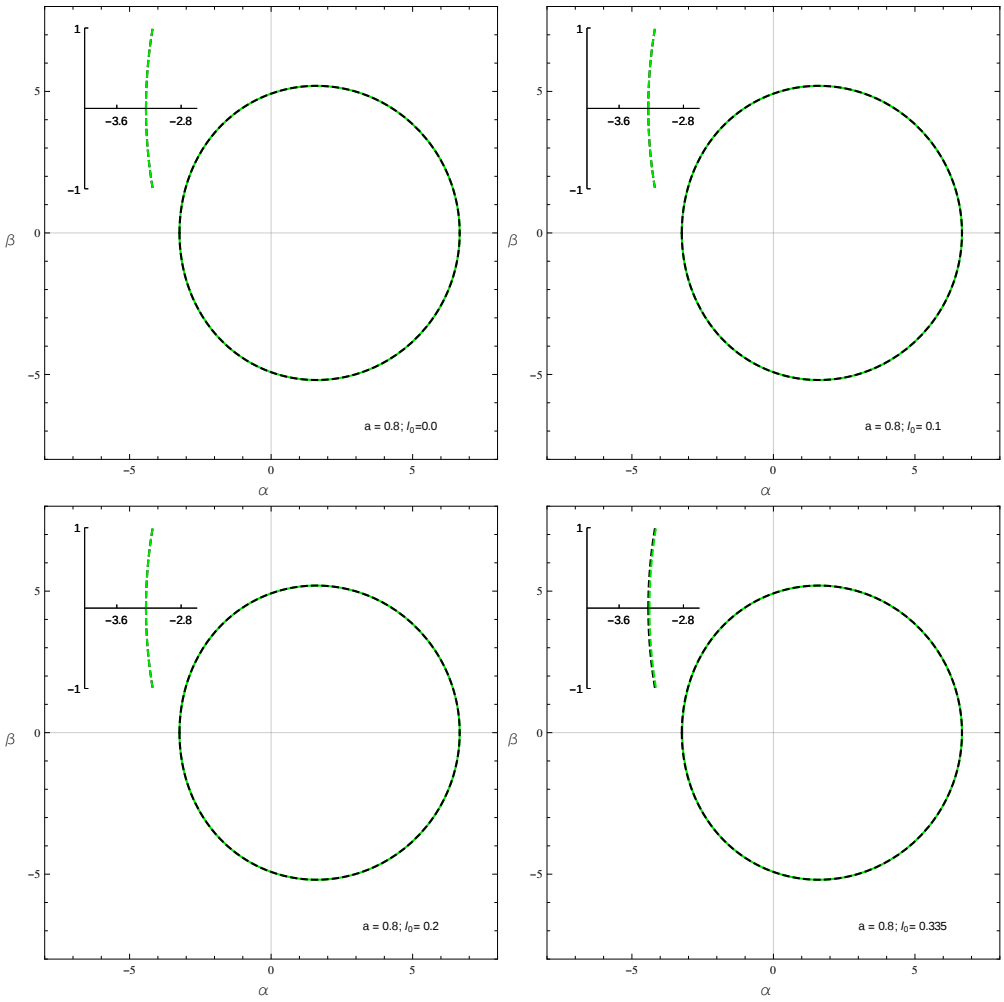

Figure 4.5: Same as in Fig. (4.4) with higher spin parameter.

Although only shadows for an inclination of $i = \pi/2$ were drawn, the deviation of the shape form the circle decreases with a smaller inclination angle as shown in Fig. (4.6) and the impact of this parameter has been vastly studied in the literature, see for instance Refs. [51, 12, 57].

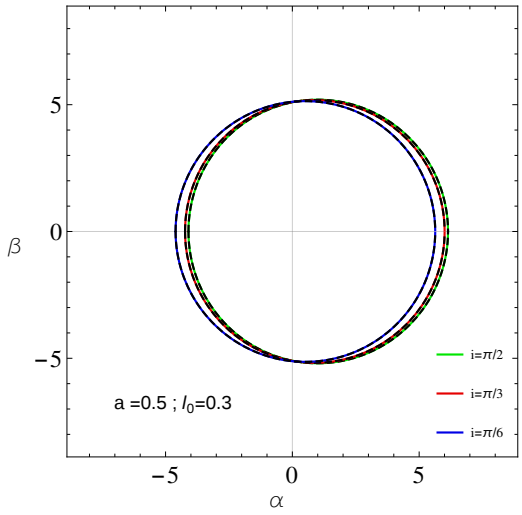

Figure 4.6: Shadows of the Kerr and "Kerrr" black holes for various values of inclination i. The celestial coordinates (α, β) are measured in the unit of the black hole mass M, $a = 0.5$ and $l_0 = 0.3$.

Since it is of particular interest to investigate how the shadow of black holes gets deformed in the case of distorted ones it has been recently an active field of research. In Refs. [41, 51, 4, 12, 101, 57, 7, 8, 73, 93, 86, 45, 64, 79, 83, 71, 100] can be found examples of black hole shadows in various theories of gravity.

Chapter 5

Relativistic Ray Tracing

The size and shape of the black hole's shadow is determined by the photon orbit, were studied in Chapters (2) and (3) and depend only on the black hole physical parameters. However, the appearance (spatial extent, shape, brightness distribution, etc.) of a "physical" image depends not only on black hole parameters, but also on the details of the accretion structure around it [91]. The work that has been done so far, assumes that the black hole is isolated from everything else, an assumption not met in most astrophysical scenarios [6].

In this section, an approximate analytic ion torus model associated with the family of Polish doughnuts, introduced in Refs. [1, 55], is used for a radiatively inefficient accretion flow to describe the accretion structure in Sgr A* based on Refs. [1, 91, 97] and using the Novikov-Thorne model, in which the disk is on the equatorial plane and the particles of the gas move on nearly geodesic circular orbits, i.e., Keplerian motion. The accretion disk is expected to have its inner edge at the radius of the ISCO.

5.1 The General relativitY Orbit Tracer of the Observatory of Paris (GYOTO)

The best candidate for horizon-resolving mm-VLBI observations is the supermassive black hole at the center of the Milky Way, Sgr A*. Because of its proximity, Sgr A* subtends the largest angle on the sky of any known black hole and presents a unique opportunity to observe strong-field general relativity effects. Particularly, for Sgr A* most of these details are uncertain, as for example the chemical abundances, the involved radiative processes, and the inclination of the accretion structure with respect to our point of view [21, 33, 91].

There are mainly three analytic models used to make a meaningful comparison between theory and observation:

- The radiatively inefficient advection dominated accretion flow (ADAF) model [72, 105].
- The jet model [40] .

- The torus model [91, 97].

The accretion structure around Sgr A* is most probably a radiatively inefficient advection dominated accretion flow [72].

The first developments of general relativistic ray-tracing date back to the 1970s, with works regarding the appearance of a star orbiting around a Kerr black hole [31], the derivation of an accretion disk's emitted spectrum in terms of a transfer function [30] and the computation of the image of an accretion disk around a Schwarzschild black hole [65].

In this work I use GYOTO [96], a general relativistic ray-tracing code which computes images of astronomical bodies in the vicinity of compact objects and trajectories of massive bodies in relativistic environments. GYOTO consists in launching null geodesics from an observer's screen, that are integrated backward in time to reach an astrophysical object emitting radiation. Once the photon gets inside the emitting object, the equation of radiative transfer is integrated along the computed geodesic in order to determine the value of the emitted specific intensity that will reach the observer [96]. For the disk model of this work, the integration of the equation of radiative transfer is straightforward since the values of the intensity are known analytically at each point of the disk.

GYOTO is an open source C++ code and is documented on its homepage[1].

5.1.1 Implementation

Here I will just summarize the most important concepts and features of GYOTO relevant to this work, based on Ref. [96] where this code was first described in detail.

The initial conditions, the position of the observer and the direction of incidence of the photon, allows the code to determine the tangent vector to the photon's geodesic at the observer's positions. The equations of motion, Eqns. (2.28), (2.29), (2.30) and (2.31) are solved by means of a Runge-Kutta algorithm of fourth order with an adaptive step and the integration goes until one of the following stop conditions is fulfilled:

1. The photon reaches the emitting object.

2. The photon escapes too far from the object.

3. The photon approaches too closely to the event horizon, which is defined as when the photon's radial coordinate becomes only a few percent larger than the radial coordinate of the event horizon.

Photons are launched from the observer's screen, which is assumed to be spatially at rest at $8.33\,kpc$ in a given specified solid angle.

The numerical accuracy of GYOTO is investigated in Ref. [96], where a convergence test was given.

[1] http://gyoto.obspm.fr

5.1.2 Radiative transfer

Once the null geodesics, integrated backward in time from the observer's screen, reaches the emitting object, the equation of radiative transfer must be integrated along the part of the geodesic that lies inside the emitter. In order to perform this computation, two basic quantities have to be known at each integration step in the frame of a given observer comoving with the emitting matter:

- The emission coefficient j_ν: Defined in such a way that an element of mass dm emits in directions confined to an element of solid angle $d\Omega$, in the frequency interval $(\nu, \nu + d\nu)$ and in time dt, an amount of radiant energy given by [27]:

  $$j_\nu dm d\Omega d\nu dt,$$

  and is related with the specific intensity's increment dI_νas along the geodesic

  $$dI_v = j_\nu ds \tag{5.1}$$

- The absorption coefficient α_ν, defined as follows: If the specific intensity I_v becomes $I_v + dI_v$ after traversing a thickness ds, measured by the observer, in the direction of its propagation it is written

  $$dI_v = -\alpha_\nu I_v ds, \tag{5.2}$$

  where the quantity α_ν introduced defines the absorption coefficient for radiation of frequency ν.

The cgs unit of j_ν is $[erg\, cm^{-3}\, s^{-1}\, ster^{-1}\, Hz^{-1}]$ while $\alpha_\nu$is expressed in $[cm^{-1}]$. The relativistic equation of radiative transfer is [69]

$$\frac{d\mathcal{I}}{d\lambda} = \mathcal{E} - \mathcal{A}\mathcal{I}, \tag{5.3}$$

where λ is an affine parameter along the considered geodesic, $\mathcal{I}$ is the invariant specific intensity, $\mathcal{E}$ is the invariant emission emission coefficient and $\mathcal{A}$ is the invariant absorption coefficient defined as follows:

$$\mathcal{I} \equiv \frac{I_\nu}{\nu^3}, \tag{5.4}$$

$$\mathcal{E} \equiv \frac{j_\nu}{\nu^2}, \tag{5.5}$$

$$\mathcal{A} \equiv \nu\alpha_\nu, \tag{5.6}$$

these quantities do not depend on the reference frame in which they are evaluated[2]. The relativistic equation of radiative transfer (5.3) written in the reference frame comoving with the fluid emitting the radiation reads:

[2]A nice explanation and short proof of the first invariant described here can be found in Ref. [68].

$$\frac{dI_{\nu_{em}}}{ds_{em}} = j_{\nu_{em}} - \alpha_{\nu_{em}} I_{\nu_{em}}, \tag{5.7}$$

where ν_{em} is the emitted frequency of the radiation and $ds_{em} \equiv d\lambda\nu_{em}$ is the amount of proper length as measured by the emitter. The latter expression can be integrated between some value s_0 where the specific intensity is vanishing and some position s:

$$I_\nu(s) = \int_{s_0}^{s} ds' \, e^{-\int_{s'}^{s} ds'' \, \alpha_\nu(s'')} j_\nu(s') \,. \tag{5.8}$$

The emission coefficient, j_ν, is required at any point within the torus. These quantities will be discussed in the following and are known analytically for the ion torus, so the integration (5.8) can be performed.

Before describing the standard equations of radiative processes, it is important to mention that the following analysis is a simple analytical model which does not achieve the same results of relativistic magnetohydrodynamic (GRMHD) numerical codes, where a proper radiative transfer in curved spacetimes is formulated and solved (see, for instance, Ref. [20] and references therein).

5.1.3 Spectra computation

By using the invariant intensity (5.4), the specific intensity observed by a distant observer can be related to the emitted specific intensity according to [96]

$$I_{\nu_{obs}} = g^3 I_{\nu_{em}}, \tag{5.9}$$

where

$$g \equiv \frac{\nu_{obs}}{\nu_{em}} \tag{5.10}$$

and is called the redshift factor.

However, a more important quantity from the observational point of view is flux density, or here, the flux (F_ν, F) which gives the power of radiation per unit area and its dimension depends on whether if the considered quantity is the flux density at a certain frequency or about the total flux density.

The observed flux F_ν is related to the observed specific intensity according to

$$dF_{\nu_{obs}} = I_{\nu_{obs}} \cos\theta d\Omega,$$

where Ω is the solid angle under which the emitting element is seen and θ is the angle between the normal to the observer's screen and the direction of incidence, the flux is given by

$$F_{\nu_{obs}} = \sum_{pixels} I_{\nu_{obs},pixel} \cos(\theta_{pixel}) \, \delta\Omega_{pixel}, \tag{5.11}$$

where $I_{\nu_{obs},pixel}$ is the specific intensity reaching the given pixel, θ_{pixel} is the angle between the normal to the screen and the direction of incidence corresponding to this

pixel and $\delta\Omega_{pixel}$ is the element of solid angle covered by a pixel in the sky, defined as the total solid angle covered by the screen divided by the number of pixels:

$$\delta\Omega_{pixel} = \frac{2\pi\,(1-\cos f)}{N^2}. \tag{5.12}$$

5.2 Ion tori

> "Accretion is the very process that allows black hole sources to emit electromagnetic radiation and other forms of energy. Because black holes are so small in size compared to the spatial scale of their sources of fueling, and because centrifugal forces on matter of given angular momentum increase more rapidly ($\propto R^{-3}$) than gravity ($\propto R^{-2}$) as one moves inward in radius R, accretion is generally believed to be a process involving rotationally supported flows. Matter in such a flow must lose angular momentum in order to move inward and release gravitational binding energy. It is the nature of the angular momentum loss mechanism, and the process whereby gravitational binding energy is converted into observable forms of energy, that are the two central questions of black hole accretion theory." [39]

Ion tori are geometrically thick, optically thin accretion structures with constant specific angular momentum. They are the optically thin counterparts of the optically thick Polish doughnuts [1, 2]. The physics of the radiative transfer used for the ion torus is based on Ref. [91] and in the following I will summarize these author's descriptions.

5.2.1 Fluid torus of constant specific angular momentum and isotropic magnetic field

GYOTO implements an accretion torus-shaped, barotropic, stationary disk of negligible self-gravitation[3], with axisymmetry and constant angular momentum with isotropic (i.e., chaotic) magnetic field around the black hole. Modeling the fluid as a "perfect-like" one, the stress energy tensor is

$$T_{\mu\nu} = (\epsilon + P)\, u_\mu u_\nu + P g_{\mu\nu}, \tag{5.13}$$

where P is the fluid pressure and ϵ is the fluid proper energy density. The fluid 4-velocity is assumed to be purely circular, i.e.,

$$u^\mu = u^t\,(1, 0, 0, \Omega)\,,$$

[3]The deviation induced by the presence of an accretion disk is usually completely negligible, because the disk mass is many orders of magnitude smaller than the mass of the black hole (see Ref. [14] for a general discussion, in which the effect of a massive accretion disk in the measurement of the black hole spin with a simple analytical model was estimated and discussed).

using Boyer-Lindquist coordinates and where Ω is the angular velocity defined in Chap. (2). The energy-momentum conservation equation

$$\nabla_\nu T^\nu_\mu = 0,$$

leads to [91, 97]

$$\frac{\nabla_\mu P}{\epsilon + P} = -\nabla_\mu \ln(-u_t) + \frac{\Omega \nabla_\mu \xi}{1 - \Omega\xi}, \tag{5.14}$$

where ξ related to the fluid four-velocity components by Eqn. (2.26). By assuming that the fluid is barotropic, i.e., $P = P(\epsilon)$, the enthalpy function, defined as follows [91]

$$H \equiv \int_0^P \frac{dP}{\epsilon + P}, \tag{5.15}$$

permits to express the Eqn. (5.14) as

$$\nabla_\mu H = -\nabla_\mu \ln(-u_t) + \frac{\Omega \nabla_\mu \xi}{1 - \Omega\xi}. \tag{5.16}$$

If one assumes $\xi = constant = \xi_0$ within the entire torus the equation of motion (5.16) reduces to

$$\nabla_\mu H = -\nabla_\mu \ln(-u_t)$$

or

$$H = W + constant,$$

where

$$W \equiv -\ln(-u_t). \tag{5.17}$$

Assuming the normalization relation $u_\mu u^\mu = -1$ the expression (5.17) can be written

$$W(r,\theta) = \frac{1}{2} \ln\left(-\frac{g_{tt} + 2\Omega g_{t\phi} + \Omega^2 g_{\phi\phi}}{(g_{tt} + \Omega g_{t\phi})^2} \right). \tag{5.18}$$

The cusp location should be between the marginally stable (2.49) and the marginally bound (2.48) orbits, which implies that ξ_0 must obey [1]

$$\xi_{ms}(a) < \xi_0 < \xi_{mb}(a), \tag{5.19}$$

with $\xi_{ms}(a)$ and $\xi_{mb}(a)$ given by Eqn (2.26) evaluated on (2.48) and (2.49), respectively. The condition (5.19) can be written more conveniently as

$$0 \leq \lambda \leq 1,$$

where the dimensionless parameter λ is defined as

$$\lambda \equiv \frac{\xi_0 - \xi_{ms}(a)}{\xi_{mb}(a) - \xi_{ms}(a)}. \tag{5.20}$$

The isobaric surfaces coincides with the equipotential surfaces of $W(r,\theta)$. The cross-sectional shape of the equipotential surfaces is given in Fig. (5.1). Thus, imposing a specific relation between Ω and λ the equipotential surfaces $W = const$ can be found. It appears that one particular surface has a "cusp" at some $r = r_{crit}$: it crosses itself in the equatorial plane, commonly called a "Roche lobe". Equipotential surfaces contained inside this critical surface are not connected to the central object: thus, matter cannot be accreted and swallowed by the black hole. It is thus assumed that the torus physical surface coincides with this critical surface. The central point, $r = r_c$, coincides with the innermost equipotential surface and to the point of maximum pressure.

Roche lobe overflow causes dynamical mass loss from the torus to the black hole, with no need of help from viscosity.

5.2.1.1 Torus solution for a polytropic equation of state

By assuming a polytropic equation of state

$$P = K\epsilon^{1+\frac{1}{n}}, \tag{5.21}$$

where K is the polytropic constant, n the polytropic index and ϵ is the total energy density, which is the sum of the energy density ρ and internal energy Π, the the enthalpy function (5.15) can be integrated to give

$$H = (n+1)\ln\left(1 + K\epsilon^{\frac{1}{n}}\right). \tag{5.22}$$

The surface of the torus is defined by $P = 0$ [91], which corresponds, according to the equation of state (5.21), to $\epsilon = 0$ and, from enthalpy function (5.22) to $H = 0$. By defining W_s as the value of the potential W at the torus surface, H_c and W_c as the values of H and W at the torus center, Eqn. (5.17) can be written as

$$H = W - W_s, \tag{5.23}$$

which implies

$$H_c = W_c - W_s. \tag{5.24}$$

For convenience, is defined a dimensionless potential as

$$\omega(r,\theta) \equiv \frac{W(r,\theta) - W_s}{W_c - W_s} \tag{5.25}$$

and from Eqns. (5.23) and (5.24) the enthalpy function is

$$H = H_c\omega. \tag{5.26}$$

The expressions (5.22), (5.23) and (5.24) allow to write

$$\ln\left(1+K\epsilon^{\frac{1}{n}}\right)=\omega\ln\left(1+K\epsilon_c^{\frac{1}{n}}\right),$$

where ϵ_c is the energy density at the torus center. Solving for ϵ one gets [91]

$$\epsilon=\frac{1}{K^n}\left[\left(K\epsilon_c^{\frac{1}{n}}+1\right)^{\omega}-1\right]^n, \tag{5.27}$$

where K is

$$K=\frac{1}{\rho_c^{\frac{1}{n}}}e^{\left(\frac{W_c-W_s}{n+1}-1\right)}. \tag{5.28}$$

5.2.1.2 Thermodynamic quantities

For this configuration the polytropic index is set to $n=3/2$, which corresponds to the adiabatic index $\gamma=5/3$ of a non-relativistic gas with no radiation pressure which is consistent with the existence of a very optically thin medium [91]. The total pressure P is expressed as the sum of the magnetic and gas contributions, P_{mag} and P_{gas} respectively, and the radiation pressure is neglected. These pressures are assumed to be fixed parts of the total pressure [91]

$$P_{mag} = \frac{B^2}{24\pi}=\beta P \tag{5.29}$$
$$P_{gas} = (1-\beta)\,P, \tag{5.30}$$

where B is the intensity of magnetic field and $\beta\equiv P_{gas}/\left(P_{gas}+P_{mag}\right)$ measures the strength of the magnetic field[4]. The gas is assumed to be an electron gas with molecular μ weight and T_e and the pressure is written

$$P_{gas}=\frac{k_B\epsilon T_e}{m_u\mu},$$

where k_B is the Boltzmann constant and m_u is the atomic mass unit. The electron molecular weight is written

$$\mu=\frac{\epsilon}{n_e m_u}=\frac{2}{1+Y},$$

where Y us the helium abundance, which is assumed to be equal to $Y=0.25$ [72], and n_e is the electron density with respect to the energy density.

For the temperature is assumed that there exists a relation[5]

[4]This β differs from the standard $\beta'\equiv P_{gas}/P_{mag}$ used in plasma physics, which is confusingly also called β [105].

[5]This assumption is made in order to obtain a dependence with the choice of T_c, i.e. the temperature of the center of the torus, and not only on the spacetime geometry.

$$T_e = C\frac{P}{\epsilon},$$

where C is a constant, but does not take its perfect-gas value [97]. The central temperature T_c is chosen at the center of the torus and defines the constant C by

$$T_c = C\frac{P_c}{\epsilon_c}.$$

Then

$$T_e = T_c\left(\frac{\epsilon}{\epsilon_c}\right)^{n-1}, \tag{5.31}$$

which depends on the choice of T_c.

5.2.2 Radiative processes

The emission coefficients inside the torus implemented in GYOTO correspond to bremsstrahlung, synchrotron radiation and Compton processes. The following expressions are the standard formulae from the literature and were presented in Refs. [91, 72] for this particular case (see, for instance, Refs. [78, 68, 67] for extensive and general discussions of these and other mechanisms in astrophysics).

5.2.2.1 Bremsstrahlung

The rate at which energy is lost due to bremsstrahlung,

$$f_{br}^{-} = \frac{dE_{br}}{dtdV} = f_{ee}^{-} \tag{5.32}$$

is due to emission from electron-electron collisions f_{ee}^{-} which is [96]

$$f_{ee}^{-} = n_e^2 r_e^2 \alpha_f m_e c^3 F_{ee}\left(\theta_e\right),$$

where the classical radius of electron and the fine structure constants are, respectively,

$$r_e = \frac{e^2}{m_e c^2} \tag{5.33}$$

$$\alpha_f = \frac{1}{137} \tag{5.34}$$

and

$$\begin{array}{rcll} F_{ee}\left(\theta_e\right) & = & \frac{20}{9\sqrt{\pi}}\left(44-3\pi^2\right)\left(1+1.11\theta_e+\theta_e^2-1.25\theta_e^{\frac{5}{2}}\right)\theta_e^{\frac{3}{2}}; & \theta_e<1 \\ & = & 24\theta_e\left[\ln\left(2\eta\theta_e\right)+1.28\right]; & \theta_e>1 \end{array} \tag{5.35}$$

with the Euler number is given in terms of the Euler-Mascheroni constant, γ_E as

$$\eta = e^{-\gamma_E} = 0.5616 \tag{5.36}$$

and the dimensionless temperature is defined as

$$\theta_e = \frac{k_B T_e}{m_e c^2}. \tag{5.37}$$

Thus, the bremsstrahlung emission coefficient is

$$j_\nu^{br} = f_{br}^{-} \frac{1}{4\pi} \frac{h}{k_B T} e^{\left(-\frac{h\nu}{k_B T_e}\right)} \overline{G}, \tag{5.38}$$

where h is the Planck's constant, the $1/4\pi$ factor assumes isotropic emission in the emitter's frame and $\overline{G}$ is the velocity-averaged Gaunt factor given by

$$\begin{array}{rcll} \overline{G} & = & \sqrt{\frac{3}{\pi}\frac{k_B T_e}{h\nu}}; & \frac{k_B T_e}{h\nu} < 1 \\ & = & \frac{\sqrt{3}}{\pi} \ln\left(\frac{4}{\gamma_E}\frac{k_B T_e}{h\nu}\right); & \theta_e > 1 \end{array} . \tag{5.39}$$

The function (5.35) has units of $[erg^{-1}\, cm^{-3}]$.

5.2.2.2 Synchrotron radiation

The emission coefficient for synchrotron emission by a relativistic Maxwellian distribution of electrons is given by [91]

$$j_\nu^{sy} = \frac{1}{4\pi} \frac{e^2}{c\sqrt{3}} \frac{4\pi n_e \nu}{K_2\left(\frac{1}{\theta_e}\right)} M\left(x_M\right),$$

with a $1/4\pi$ factor for isotropic emission in the emitter's frame, K_2 is the modified Bessel function of second kind and the fitting function,

$$M\left(x_M\right) = \frac{4.0505\alpha}{x_M^{\frac{1}{6}}} \left(1 + \frac{0.48\beta}{x_M^{\frac{1}{4}}} + \frac{0.5316\gamma}{x_M^{\frac{1}{2}}}\right) e^{-1.8899 x_M^{\frac{1}{3}}},$$

where

$$\begin{array}{rcl} x_M & = & \dfrac{2\nu}{3\nu_0 \theta_e^2}, \\ \nu_0 & = & \dfrac{eB}{2\pi m_e c} \end{array}$$

and the parameters α, β and γ are all adjustable. In Ref. [66] appears a table of the optimized parameters at various temperatures.

5.2.2.3 Compton processes

The soft bremsstrahlung and synchrotron photons in an ion torus filled with a thermal distribution of electrons are (inverse) Compton scattered to higher energies. In the central regions of the flow in particular, this can be an important cooling mechanism [91].

There is a probability $\mathcal{P}$ that a seed photon of some initial energy, $E_{in} = h\nu$, is in optically thin material scattered to an amplified energy [91]

$$E_{out} = \mathcal{A} E_{in},$$

where

$$\mathcal{P} = 1 - e^{-\tau_{es}},$$

with the optical depth

$$\tau_{es} = \int n_e \sigma_T dl,$$

where the Thomson cross section is

$$\sigma_T = \frac{8\pi}{3}\left(\frac{e^2}{mc^2}\right)^2 \approx 6.625 \times 10^{-25} cm^2,$$

for the electron, and

$$\mathcal{A} = 1 + 3\theta_e + 16\theta_e^2.$$

The energy exchange between electrons and photons depends only on the electron temperature θ_e and the probability that a photon will interact with an electron which is given by the electron scattering optical depth. In Ref. [38] was derived an approximate prescription for the energy enhancement factor due to Compton scattering, which is defined as the average energy change of a seed photon

$$\eta = 1 + \eta_1 + \eta_2 \left(\frac{x}{\theta_e}\right)^{\eta_3},$$

where

$$\begin{aligned} \eta_1 &= \frac{\mathcal{P}(\mathcal{A}-1)}{1-\mathcal{P}\mathcal{A}} \\ \eta_2 &= 3^{-\eta_3}\eta_1 \\ \eta_3 &= -1 - \frac{\ln \mathcal{P}}{\ln \mathcal{A}}. \end{aligned}$$

The dimensionless energy is given by

$$x = \frac{h\nu}{m_e c^2}.$$

Comptonized emission is $\eta - 1$ times the seed photon distribution. The part of the spectrum that can be Comptonized lies between the critical synchrotron self-absorption edge

$$x = x_c = \frac{h\nu_c}{m_e c^2}$$

and $x = 3\theta_e$. Note that as the emerging photons cannot gain more energy than the electrons they collide with have, there is an upper limit to the energy gained

$$x \lesssim 3\theta_e.$$

Comptonization of bremsstrahlung emission is then given by

$$j_\nu^{br,C} = j_\nu^{br} 3\eta_1 \theta_e \left\{ \left(\frac{1}{3} - \frac{x_c}{3\theta_e} \right) - \frac{1}{\eta_3 + 1} \left[\left(\frac{1}{3} \right)^{\eta_3+1} - \left(\frac{x_c}{3\theta_e} \right)^{\eta_3+1} \right] \right\}. \tag{5.40}$$

Comptonization of synchrotron radiation that is emitted mostly at the self-absorption frequency ν_c is given by

$$j_\nu^{sy,C} = j_\nu^{sy} \left[\eta_1 - \eta_2 \left(\frac{x_c}{\theta_e} \right)^{\eta_3} \right].$$

5.2.2.4 Total cooling

> "All three of the processes described above are similar, since in every case the physical scenario studied to get them is dealing with the collision between a charge and a photon. What changes the mechanism is the nature of the prescattered radiation. In bremsstrahlung emission the electron plows through the virtual photon field of the ion Ze, in synchrotron the electron scatters with the virtual photons compromising the magnetic field and in Compton scattering the collision occurs between a charge and a free photon, dynamically distinct from the charge that produced it". Adapted from Ref. [68]

The total emission coefficient is the sum of all radiative contributions

$$j_\nu = j_\nu^{br} + j_\nu^{br,C} + j_\nu^{sy} + j_\nu^{sy,C}. \tag{5.41}$$

For a medium in local thermodynamic equilibrium (LTE) at temperature T, the emission coefficient given in Eqn. 5.41 and the absorption coefficient are related by means of Kirchhoff's law

$$\alpha_\nu = \frac{j_\nu}{B_\nu(T)} \tag{5.42}$$

where B_ν is Planck's law of blackbody radiation

$$B_\nu = \frac{2h\nu^3}{c^2}\frac{1}{e^{\frac{h\nu}{K_B T}} - 1}. \tag{5.43}$$

However, since for the typical optical depth of ion tori, α_ν is negligible, the absorption is ignored and assumed zero everywhere. Integration of j_ν over the whole frequency range gives the total cooling rate at each point (r, θ) in the torus. Radiation that originates close to a black hole is influenced by various relativistic effects, such as the gravitational bending of light rays, gravitational redshift, and Doppler beaming [91]. GYOTO ray-traces the emission derived in Eqn. (5.41) from each point (r, θ) inside the so-called Roche lobe equipotential back to the observer explicitly including all relativistic effects in light propagation.

5.3 Adding the "Kerrr" metric to GYOTO

According to Frédéric Vincent (private communication) writing a plugin is the "cleanest" way to modify GYOTO and perhaps not the "simplest". In order to use the "Kerrr" metric for the calculation a new Metric was added. The steps followed were:

- Create the files lib/KerrrRBL.C, include/GyotoKerrrRBL.h from the lib/KerrRBL.C, include/GyotoKerrRBL.h implemented already in GYOTO, by modifying the functions needed, in particular:
  - The metric coefficients, in covariant and contravariant form,
  - the prograde Marginally Stable orbit,
  - the prograde Marginally bound orbit,
  - the potential,
  - the specific angular momentum,
  - the standard equations of geodesics and
  - the circular velocity.
- Update the file lib/Makefile.am by adding KerrrBL.C when defining the variable libgyoto_stdplug_la_SOURCES
- Update lib/StdPlug.C by adding a #include "GyotoKerrrBL.h" and Metric::Register("KerrrBL", &(Metric::Subcontractor<Metric::KerrrBL>));
- Build up the whole code in order to get shared libraries files.

The polish doughnut was not modified and follows completely the above description, since the model is formulated for a generic stationary and axisymmetric spacetime as the one described in Chap. (3). If the background metric is known, there is only one unspecified function, (3.23), which characterizes the fluid's rotation. Thus, GYOTO

integrates backward in time the null geodesics from the observer's screen to reach the torus emitting radiation and then the equation for radiative transfer is integrated along the modified computed geodesic in order to determine the value of the emitted specific intensity that will reach the observer. For the "Kerrr" spacetime the quantities mentioned above, i.e., prograde Marginally Stable orbit, prograde Marginally bound orbit, potential and circular velocity were first calculated numerically and the value plugged into the code. However, as it was shown in Chap. (3), those values are very similar to the Kerr values.

5.4 The black hole silhouette with ion tori

So far the torus is characterized by the black hole spin, a, and inclination of the spin axis to the line of sight, i, the torus angular momentum, λ, the polytropic index, n , the magnetic total pressure ration, β, and the central values of density, ϵ_c, and electron temperature $T_{e,c}$.

The specific intensity at any point within the torus is obtained as follows:

1. From λ and a one evaluates ξ_0 via Eqn. (5.20).
2. With the values of ξ_0 and a the potential $W(r,\theta)$, Eqn. (5.18), is fully determined, using Eqn. (3.23) and the value found above.
3. Now, in order to get a Roche-lobe filling torus, the value W_s of the potential W a the torus surface must be set to the value at the Roche love as follows
$$W_s = W\left(r_{in}, \frac{\pi}{2}\right).$$
4. The value H_c is obtained from Eqn. (5.22).
5. Given W_s and $H_c$the value W_c can be obtained from Eqn. (5.24).
6. The dimensionless potential $\omega(r,\theta)$ is obtained from Eqn. (5.25).
7. The energy density is obtained from Eqn. (5.27).
8. The temperature can be found with the previous value from Eqn. (5.31).
9. The value of the total cooling is obtained from Eqn. (5.41).
10. The specific intensity is obtained finally by direct integration of Eqn. (5.8) along the null geodesic that lies inside the emitter.

5.4.1 Images

The quantity that is carried along the geodesic computed by GYOTO is the specific intensity I_ν, with units $[erg\,cm^{-2}\,s^{-1}\,ster^{-1}\,Hz^{-1}]$, updated at each step inside the torus by using Eqn. (5.1). The image is then defined as a map of specific intensity

Parameter		Value
Angular Momentum	λ	0.3
Magnetic Pressure Ratio	β	0.1
Polytropic Index	n	$3/2$
Central Density $[g\,cm^{-3}]$	ϵ_c	10^{-17}
Central Electron Temperature	$T_{e,c}$	$0.02\,T_{vir}$

Table 5.1: Parameters for the reference ion torus. T_{vir} is the virial temperature. This parameters can be compared with table 1 of Ref. [91].

[96]: each pixel of the screen contains one value of I_ν that can be plotted. However, this is not an "real" image, i.e., the one that would be obtained with a telescope, since a real image is a map of specific fluxes values, and a specific flux is the sum of the specific intensity of some solid angle. So the GYOTO screen is considered to be point-like, where a pixel corresponds to a direction of the sky.

The images (Figs. (5.2), (5.4) and (5.5)) are maps of specific intensity I_ν of an ion torus surrounding a Schwarzschild, Kerr and "Kerrr" black holes. Table (5.1) gives the reference values of the parameters used for the computations, specifically chosen for comparison with Ref. [96]. For all images the frequency shown is $10\,Hz$ and is just for reference.

Each image is a superposition of a first-order image, i.e., the thick distorted image, and highe-order images, i.e., the "circles" centered on the black hole, produced by photons that swirl around the black hole before reaching the observer. The very fine circles of light consist of photons originating from a location just outside the photon orbit, see Chap. (2) for details. In these images the black hole silhouette is produced by the photons, which are severely red-shifted, that escape from the region inside the photon orbit and create an area of reduced intensity on the observer's screen [91].

According to Ref. [83] the half opening angle of the shadow, as measured by different observers at infinity and for black holes with different spins, is always equal to

$$(5 \pm 0.2)\,\frac{GM}{Dc^2}, \tag{5.44}$$

where M is the mass of the black hole and D is the distance from the Earth. For the supermassive black hole Sgr A* at the Galactic center they are [44]

$$M = 4.3 \times 10^6\, M_\odot$$

and

$$D = 8.3\,kpc.$$

Based in this result I will provide an estimate size of the images produced by GYOTO in terms of (5.44). Using the image shown in (5.2), whose size $400 \times 400\,pixels$, I analyze the magnitude of intensity of the accretion flow image on the two-dimensional image plane of an observer located at Earth along the three cross sections delineated

by the dashed lines, see Fig. (5.3). As expected, the steepest points occur at the brightest points in the image, which will be considered the rim of the black hole shadow. Note, however, that fainter and larger rims appear also at the outer edges of the image.

The shadow size, in pixels, was calculated numerically from Fig. *Right* (5.3), where the dashed red line was drawn. This value was converted, using Eqn. (5.44), to a more physical presentation, see Fig. (5.4) for Kerr black holes and Fig. (5.5) for "Kerrr" black holes. One can also write the approximate dimensions of the image in other units, e.g., $\mu arcs$, however, as it was discussed above, the images shown are not physical images at all, and that is the reason why I have draw the images in $[M]$ which is just a scale factor.

Knowing the particular extent and shape of the accreting region from observations will allow to constrain various parameters of the flow. As expected, the differences found in Figs. (5.4) and (5.5) are negligible.

5.4.2 Spectra

Figures (5.6) and (5.7) show the resulting emitted spectra, by using Eqn. 5.11, for the Kerr and "Kerrr" black holes seen under different angles[6]. To produce these spectra, 50 values of observed frequencies were considered, evenly spaced logarithmically, between 10^5 and $10^{25} Hz$. Note that the results are shifted with respect to the ones presented in Ref. [91], since I have used the temperature for the accretion torus defined in Ref. [97].

The left panel of Fig. (5.6) shows the total spectrum, while the right panel shows the contributions from the emission mechanisms under consideration, i.e. bremsstrahlung, synchrotron emission, and inverse Compton scattering of both bremsstrahlung and synchrotron photons.

These figures show that the ion torus model is able to account for the general features of the observed data, which is fitted for the millimeter spectrum in Ref. [97], by the parameters chose. This includes the X-ray flare "bow tie" which in the ion torus model may originate from soft photons that are inverse Compton scattered by the same population of hot electrons that is responsible for the synchrotron emission [91]. However the flattening of the spectrum at low frequencies is not matched by this model, which is due to the absence of a non-thermal electron distribution[7].

5.4.2.1 χ^2 Analysis

The following analysis emulate the standard technique used in Ref. [56], which is suitable for X-ray data, but here is just performed as a numerical experiment for the

[6]Since observed flux densities are usually rather small, especially in radio astronomy, the flux is presented in νF_ν.

[7]A more evolved model taking into account this effect was developed recently in Ref. [97], where a millimeter-wavelength synchrotron radiative model for Sgr A* based on the fully general relativistic, analytical magnetized torus model of Komissarov [61] .

sake of comparison, consisting of grouping the data to a minimum n of counts per bin.

In order to compare the profiles shown in Figs. (5.6) and (5.7), I consider the Kerr model with spin parameter $a/M = 0.4$ and inclination angle $i = \pi/2$, with notation

$$n_j^{Kerr},$$

to indicate the photon flux number density in the frequency $[\nu_j, \nu_j + \Delta\nu_j]$ of the spectrum profile, and the comparison model as a "Kerrr" black hole with noncommutative parameter $l_0/M = 0.3$, spin parameter $a/M = 0.4$ and inclination angle $i = \pi/2$ with, correspondingly, a profile

$$n_j^{"Kerrr"}.$$

The comparison is be made using the normalized log-likelihood, $\mathcal{L}$, introduced in Ref. [56], as

$$\mathcal{L} = \frac{1}{\sum_i n_i^{Kerr}} \left[\sum_j \frac{\left(n_j^{Kerr} - \alpha n_j^{"Kerrr"}\right)^2}{n_j^{Kerr}} \right], \tag{5.45}$$

where α is

$$\alpha = \frac{\sum_j n_j^{"Kerrr"}}{\sum_j \left(\frac{\left(n_j^{"Kerrr"}\right)^2}{n_j^{Kerr}} \right)}.$$

Then, the corresponding χ^2 is

$$\chi^2 \approx N\mathcal{L}, \tag{5.46}$$

where N is the number of detected photons. The relation of χ^2 and $N\mathcal{L}$ is only approximate and becomes exact in the limit of high counts.

Table (5.2) shows the χ^2 for different values of N and n. The value $N = 10^3$ corresponds to a high-quality observation today, and $N = 10^5$ is an optimistic benchmark for quality observation with next generation missions, e.g., for X-ray satellite [56][8]. The difference obtained is near to the so-called *machine epsilon* of the computer used in the calculations, which is $2.22044604925e - 16$, corresponding to a floating-point computer numbering format that occupies 8 bytes (64 bits) in computer memory, which means that the numerical errors calculating the χ^2 became too big.

However, it is important to point out that the spectra shown in Figs (5.6) and (5.7) are indeed different, and the difference appears due to the introduction of the noncommutative parameter, since the numerical values of the the quantity νF_ν are below of the machine epsilon for all the cases, but the standard χ^2 procedure can not be applied to these subtle differences.

[8]These values refer to the photon count number in the iron line of a typical measurements, which has nothing to do with the radiation emitted by a ion torus, and here was used just as a rough numerical experiment.

N	n	χ^2
10^5	10	$6.5380311554182026e-16$
	20	$6.5380224229632192e-16$
10^3	10	$6.2236458883078157e-18$
	20	$6.1029550612365413e-18$

Table 5.2: Values of χ^2 for different values of N and n. See the text for more details.

It is challenging to test the Kerr metric of black hole candidates because most measurements cannot distinguish a Kerr black hole from a non-Kerr black hole with a different spin parameter, namely there is a degeneracy between the spin and possible deviations from the Kerr solution. In the case of Sgr A^*, in the near future it will be probably possible to have different measurements, which are sensitive to different relativistic effects, of the same object. If combined together, we can hope to be able to break the parameter degeneracy [9]. Here, I just showed the effect of the spin parameter a and of the noncommutative parameter l_0 describing possible deviations from the Kerr geometry. However, the impact of l_0 is again very small, meaning that a measurement cannot provide an independent estimate of the two parameters or will allow to break the degeneracy.

[9]The analysis of the iron $K\alpha$ line is other technique, not discussed in this work, which has a more complicated structure and it is potentially a more powerful tool to test the Kerr metric, see for instance Ref. [56].

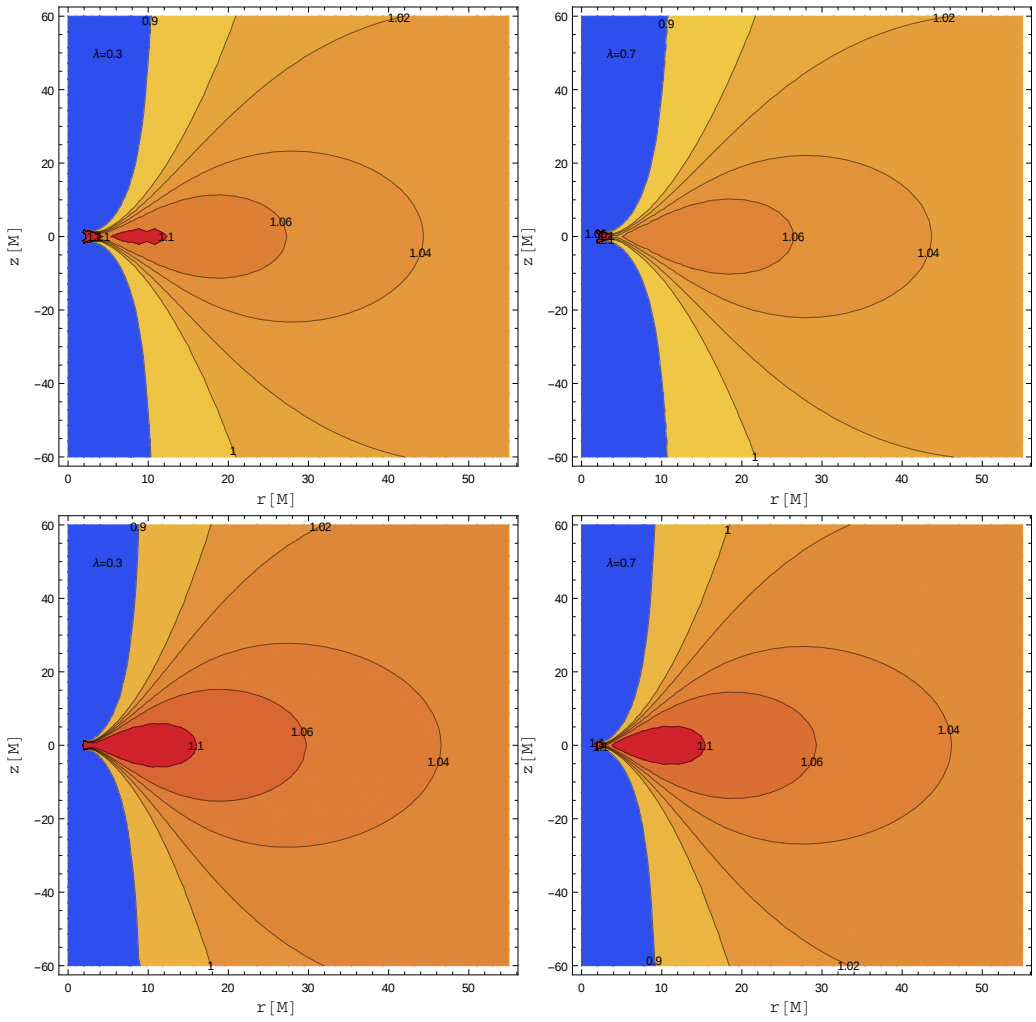

Figure 5.1: Meridional cuts through a $\lambda = 0.3$ and $\lambda = 0.7$ around a black hole. (*Top panels*) Schwarzschild case. (*Bottom panels*) Kerr case with a $a = 0.5\,M$. Note that the surfaces of constant pressure, which represent the possible boundaries of the fluid configuration. The numbers on the curves refer to different values of W. This figures can be compared with Fig. 1 of Refs. [1, 91].

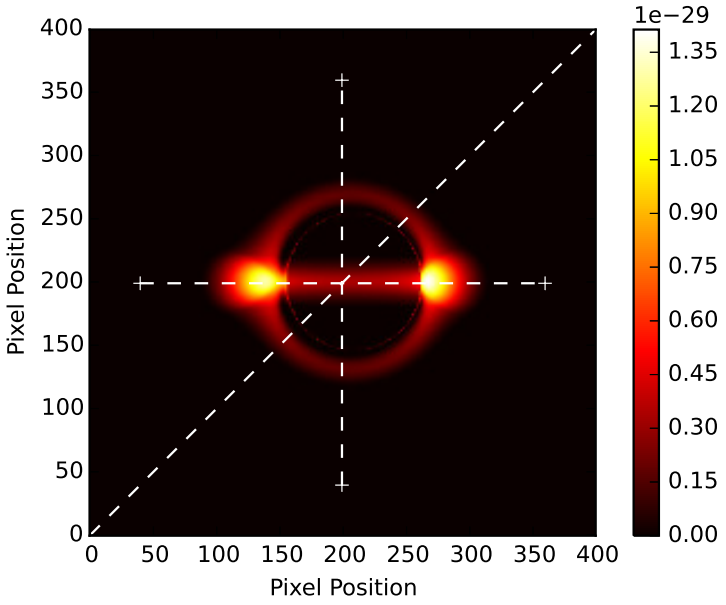

Figure 5.2: False-colour image of a ion torus around a Schwarzschild black hole with 400×400 pixels screen. The inclination of the observer is set to $\pi/2$ with respect to the angular momentum vector of the accretion flow. The dashed lines show three cross sections at 0, $\pi/4$ and $\pi/2$ with respect to the equatorial plane. All the parameters are set to their reference values listed on Table 5.1.

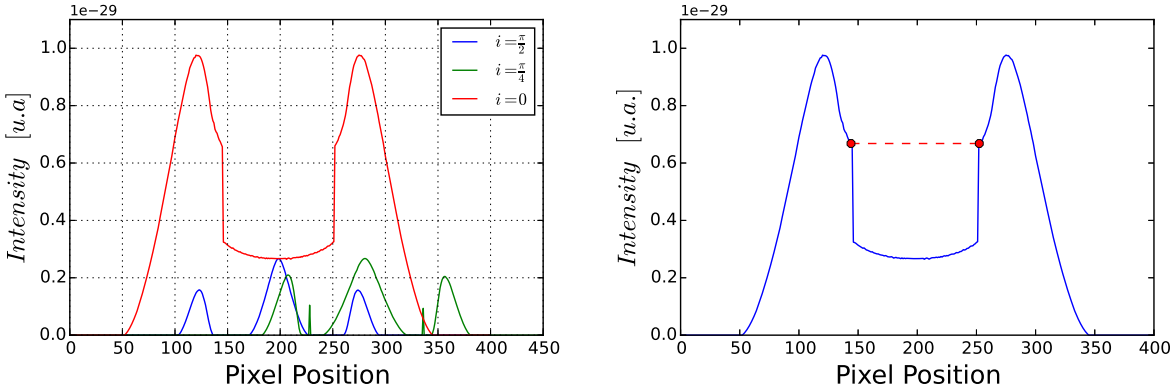

Figure 5.3: (*Left*) The brightness of the image shown on the Fig. (5.2) along the three indicated cross sections. In all cases the rim of the black hole shadow corresponds to the sharp drop in the brightness. (*Right*) The brightness of the image shown on the Fig. (5.2) along the 0 cross section, which better allows to calculated, numerically, the rim of the black hole shadow.

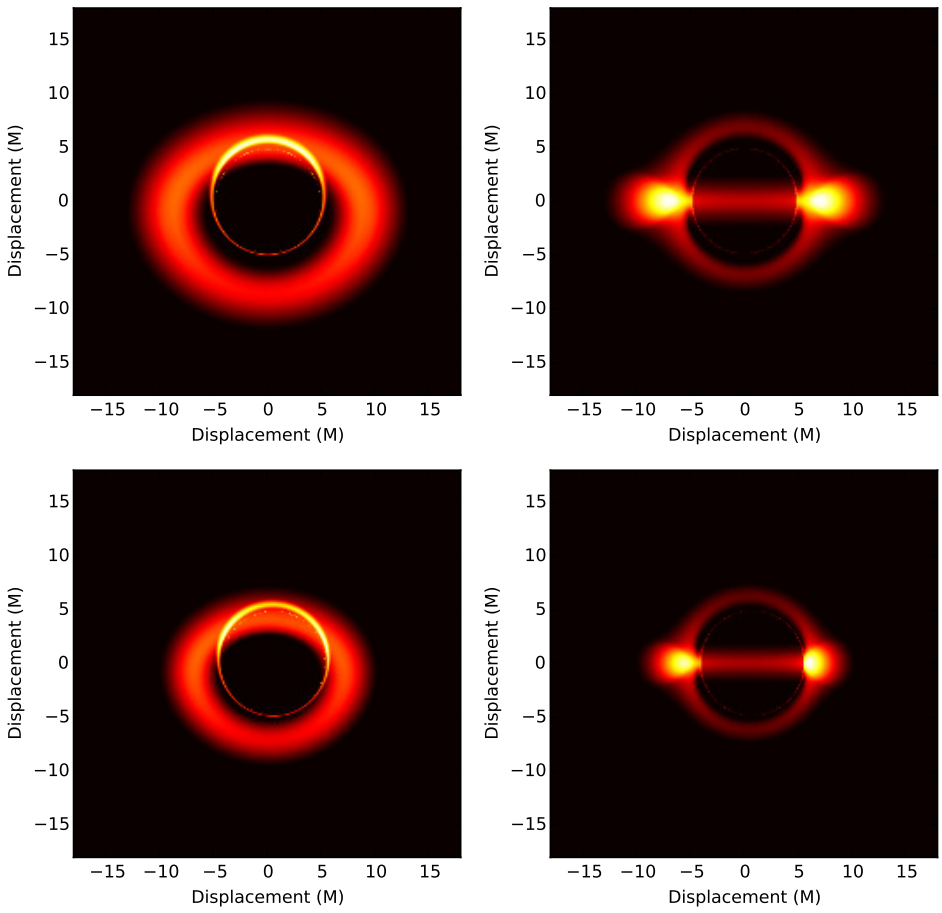

Figure 5.4: False-colour images of the reference ion torus corresponding to the parameters listed on Table 5.1, as observed by an observer on Earth. *Top panels:* Schwarzschild case. (*Upper left*) Inclination angle $i = \pi/4$. (*Upper right*) Inclination angle $i = \pi/2$. *Bottom panels:* Kerr case with $a = 0.4\,M$. (*Lower left*) Inclination angle $i = \pi/4$. (*Lower right*) Inclination angle $i = \pi/2$.

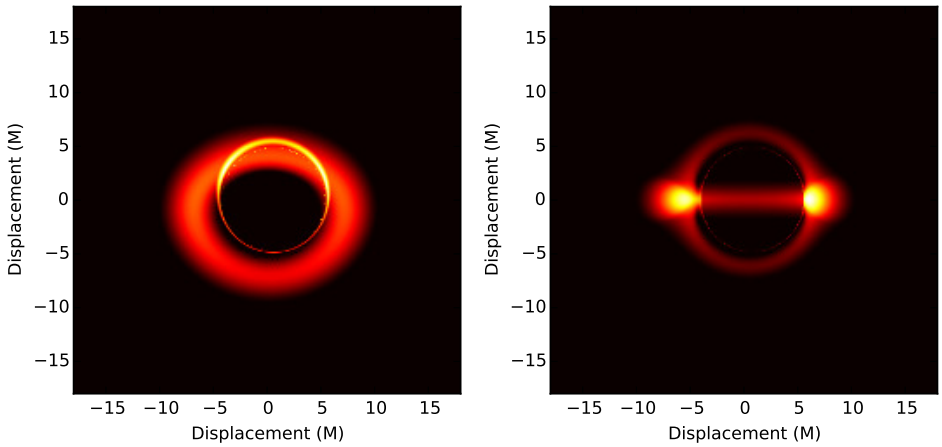

Figure 5.5: False-colour images of the reference ion torus corresponding to the parameters listed on Table 5.1, as observed by an observer on Earth in the "Kerrr" geometry with $a = 0.4\,M$ and $l_0 = 0.3\,M$. (*Left*) Inclination angle $i = \pi/4$. (*Right*) Inclination angle $i = \pi/2$.

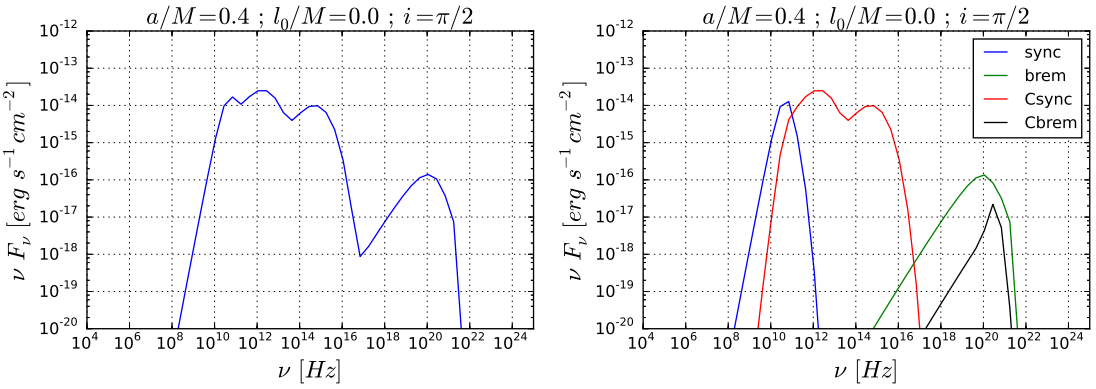

Figure 5.6: (*Left*) Spectrum of the ion torus, showing the quantity νF_ν for different values of frequencies. All the parameters not shown in the figures are set to their reference values listed on Table 5.1. (*Right*) Contribution from every radiative mechanism, namely bremsstrahlung emission, Comptonization of bremsstrahlung emission, synchrotron radiation, and Comptonisation of synchrotron radiation.

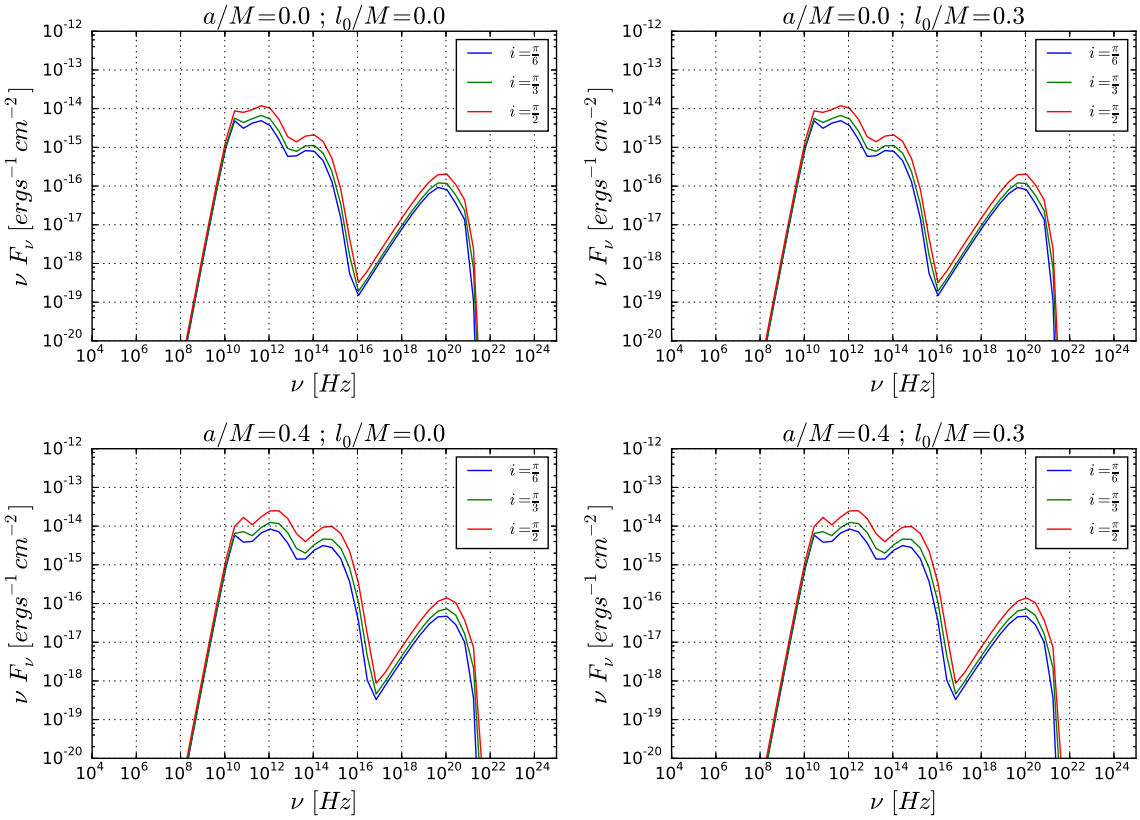

Figure 5.7: The spectra show the quantity νF_ν for different values of frequencies. The impact of inclination, i, spin, a/M and the noncommutative parameter l_0/M are shown in each figure. All other parameters are set to their reference values listed on Table 5.1. The shape of the figures can be compared with figures 4 and 9 of Ref. [91].

Chapter 6

Observables

6.1 Parameters

6.1.1 The radius R_s and the distortion parameter δ_s

The size and the form of the shadow can be characterized by using the two observables introduced in Ref. [51]. The observable R_s is defined as the radius of a reference circle passing by three points of the shadow: the top position (α_t, β_t), the bottom position (α_b, β_b), and the point corresponding to the unstable retrograde circular orbit seen by an observer on the equatorial plane $(\alpha_r, 0)$, see Fig. (6.1). The distortion parameter δ_s is defined by the quotient D/R_s, where D is the difference between the end points of the circle and of the shadow, both of them at the opposite side of the point $(\alpha_r, 0)$, i.e., corresponding to the prograde circular orbit [51, 4].

The radius R_s gives an idea of the approximate size of the shadow, while δ_s measures its deformation with respect to the reference circle (for more details, see Refs. [51]). However in this case a dark "lunate" shadow is observed, which can be approximate by the arc with the radius R_a and the central angle θ_c as is also defined in [51] for naked singularities, but here not analyzed.

In the case of Kerr backgrounds, the exact shape of the shadow depends only on the black hole spin parameter, a, and the line of sight of the distant observer with respect to the black hole's spin, i. For a given inclination angle i, there is a one-to-one correspondence between a and the distortion parameter δ_s [64]. If one has an independent estimate of the viewing angle and measures the distortion parameter of the shadow it can be inferred its spin parameter a [51]. Figs. (6.2) and (6.3) show the curves describing the spin parameter a/M as a function of the distortion parameter δ_s for different black holes and different inclination angles.

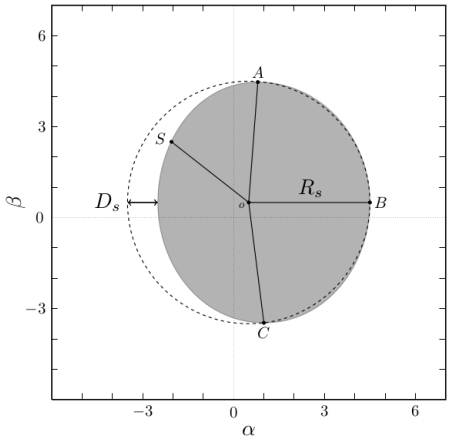

Figure 6.1: Black Hole's shadow with the three parameters that approximately characterize its shape: the radius R_s, the dent D_s, and the distance S. R_s is defined as the radius of the circle passing through the points A, B and C, located at the top ($\beta = \beta_{max}$), most right end of the shadow and bottom, respectively. D_s is the difference between the most left points of the circle and of the shadow. S is the distance between the center of the circle, O, and the most left end of the shadow at $\beta = \beta_{max}/2$. The Hioki-Maeda distortion parameter is $\delta_s = D_s/R_s$ [51]. The Tsukamoto-Li-Bambi distortion parameter is $\epsilon = S/R_s$ [93]. α and β in units $M = 1$. See the text for more details. Figure courtesy of D. Torres.

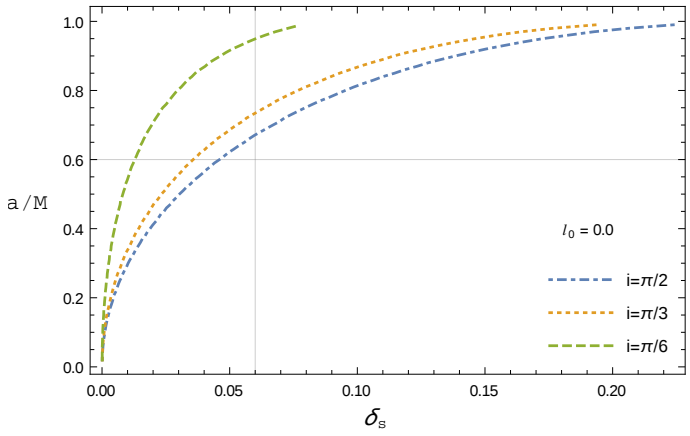

Figure 6.2: The distortion δ_s of the black hole shadow against spin a for different values of inclination angle i in the Kerr geometry. The lines presented are just for reference.

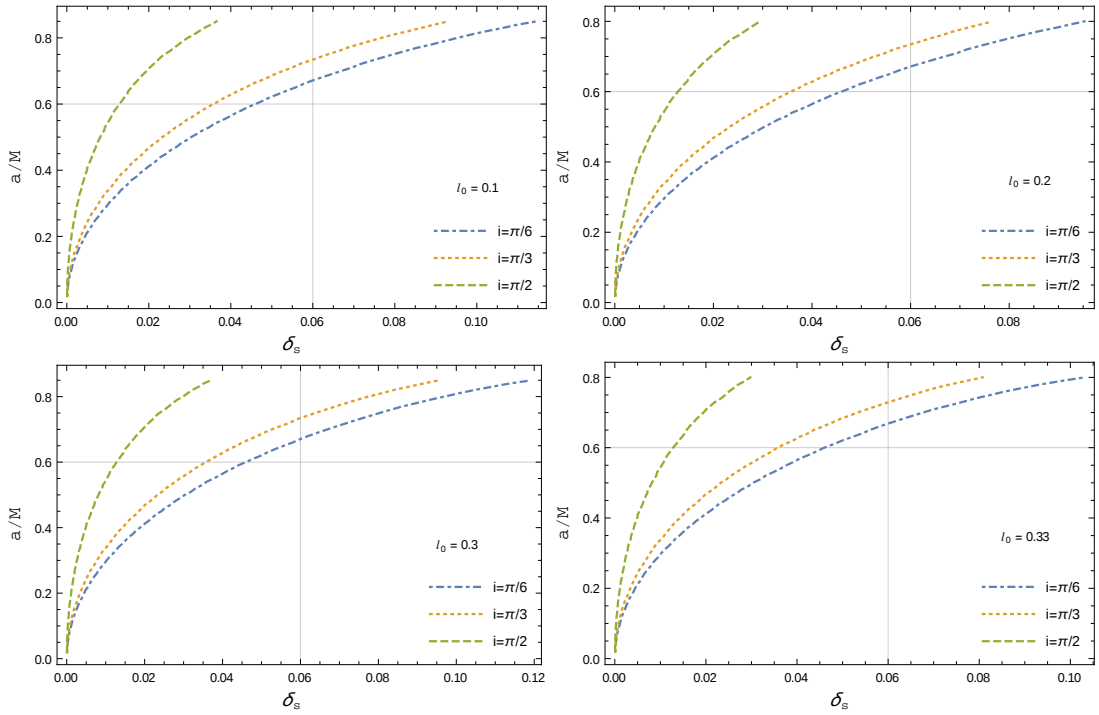

Figure 6.3: The distortion δ_s of the black hole shadow against spin a for different values of inclination angle i and noncommutative parameter l_0. The lines presented are just for reference. This figure can be compared with figure 5 of Ref. [100].

In order to compare it with that of the Kerr black hole, the difference $\delta_{s_{Kerr}} - \delta_{s_{Kerrr}}$ was plotted, see Fig. (6.4), and it can be seen that significant differences start from $l_0 = 0.3$ with differences of about 0.1%, as were reported first in Ref. [100]. Adopting the results presented in Ref. [83] for the half opening angle of the shadow, as measured by different observers from Earth, this difference, for Sgr A*, will be less than$\sim 10^{-3}\,\mu arcs$.

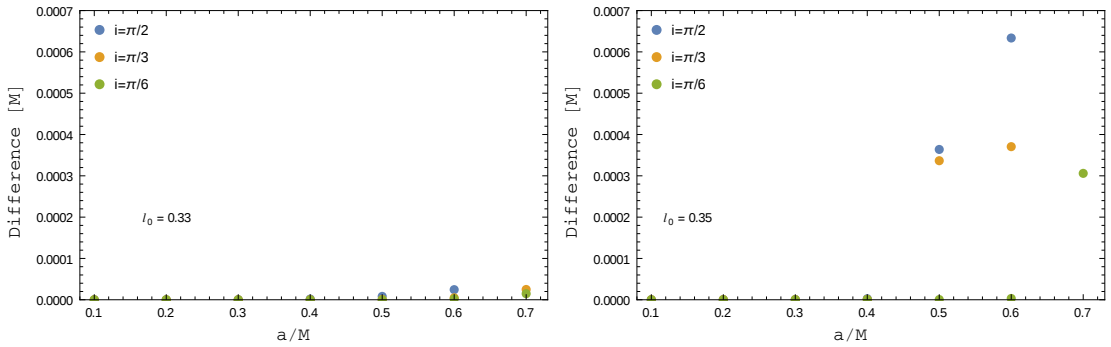

Figure 6.4: The distortion δ_s of the black hole shadow against spin a for different values of inclination angle i and noncommutative parameter l_0.

6.1.2 The distortion parameter ϵ

In Ref. [93] was pointed out, by studying the fine structure of the shadow, that the main difference in the shadow shape is in the apparent photon capture radii on the side corresponding to the ones associated to co-rotating orbits and there was defined another distortion, ϵ, as follows. With reference to Fig. (6.1), S is defined as the distance between the center of the circle of the shadow, O, and the point on the right side of the boundary with coordinate $\beta = \beta_{max}/2$, where β_{max} is the β coordinate of the top end of the shadow used to find R_s. The third observable is defined as $\epsilon = S/R_s$ which, like the Hioki-Maeda distortion parameter δ_s, only depends on the shape of the shadow.

The distortion parameter ϵ as a function of the spin parameter a/M for different black holes is shown in Fig. (6.5) and (6.6)

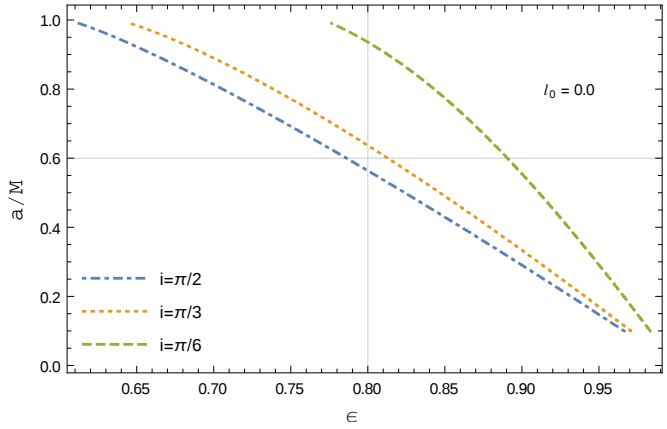

Figure 6.5: The distortion ϵ of the black hole shadow against spin a for different values of inclination angle i in the Kerr geometry. The lines presented are just for reference.

Note that the shapes of the shadows of Kerr and "Kerrr" black holes are extremely similar and therefore only very accurate image can distinguish the two metrics and provide a meaningful constraint on l_0.

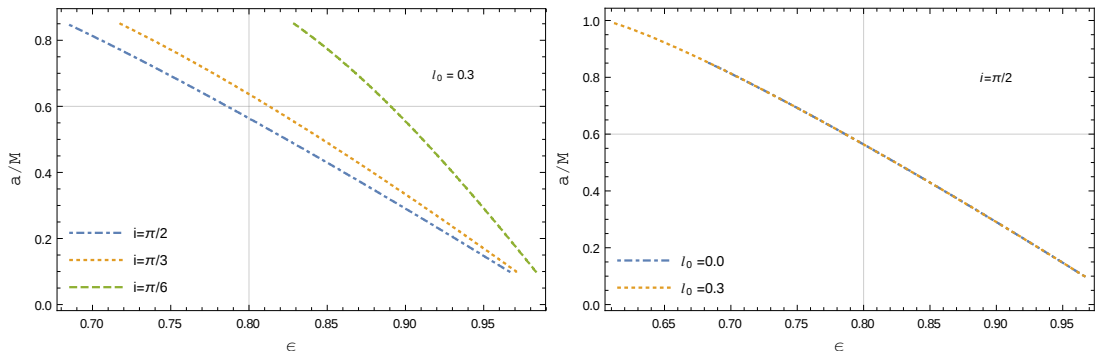

Figure 6.6: The distortion ϵ of the black hole shadow against spin a for different values of inclination angle i and noncommutative parameter l_0. The lines presented are just for reference. This figure can be compared with figure 5 of Ref. [100].

6.2 Addendum: Shadow Detection with Image Gradients

Inspired by the edge detection scheme for interferometric data and pattern matching algorithm presented in Ref. [83], I analyze the images presented in Sec. (5.4.1) in order to detect sharp features (edges) in a model-independent fashion, by applying the gradient method[1] [23, 80] and the Hough transform [37, 52, 53].

6.2.0.1 Canny's Method

The discontinuities are abrupt changes in pixel intensity which characterize boundaries of objects in a scene. Classical methods of edge detection involve convolving the image with an operator (a 2-D filter), which is constructed to be sensitive to large gradients in the image while returning values of zero in uniform regions [80, 94].

- Smooth the image using a Gaussian with sigma width:

$$G(x,y) = \frac{1}{2\pi\sigma^2} e^{-\frac{x^2+y^2}{2\sigma^2}}, \tag{6.1}$$

  where σ is the standard deviation of the Gaussian, which influence highly the detection results. The Gaussian outputs a "weighted average" of each pixel's neighborhood, with the average weighted more towards the value of the central pixels.

- Apply the horizontal and vertical Sobel operators to get the gradients within the image. The edge strength is the norm of the gradient. The operator consists of a pair of 3×3 convolution kernels

[1] This kind of algorithms has been already applied to interferometric images to quantify properties of the turbulent structure of the interstellar magnetic field, see for instance Ref. [43].

$$G_x = \begin{matrix} -1 & 0 & 1 \\ -2 & 0 & 3 \\ -1 & 0 & 1 \end{matrix} \quad G_y = \begin{matrix} 1 & 2 & 1 \\ 0 & 0 & 0 \\ -1 & -2 & -1 \end{matrix}, \tag{6.2}$$

designed to respond maximally to edges running vertically and horizontally relative to the pixel grid, one kernel for each of the two perpendicular orientation. The kernels can be applied separately to the input image, to produce separate measurements of the gradient component in each orientation. These can then be combined together to find the absolute magnitude of the gradient at each point and the orientation of that gradient. The gradient magnitude is given by:

$$|\nabla f(x,y)| = \sqrt{(\partial_x f(x,y))^2 + (\partial_y f(x,y))^2}. \tag{6.3}$$

- Thin potential edges to 1-pixel wide curves. First, find the normal to the edge at each point. This is done by looking at the signs and the relative magnitude of the X-Sobel and Y-Sobel to sort the points into 4 categories: horizontal, vertical, diagonal and antidiagonal. Then look in the normal and reverse directions to see if the values in either of those directions are greater than the point in question. Use interpolation to get a mix of points instead of picking the one that's the closest to the normal.

- Perform a hysteresis thresholding: first label all points above the high threshold as edges. Then recursively label any point above the low threshold that is 8-connected to a labeled point as an edge.

Fig. (6.7) shows the result of the Canny's edge detection algorithm applied to the (*Lower left*) image of Fig. (5.4) for different values of σ.

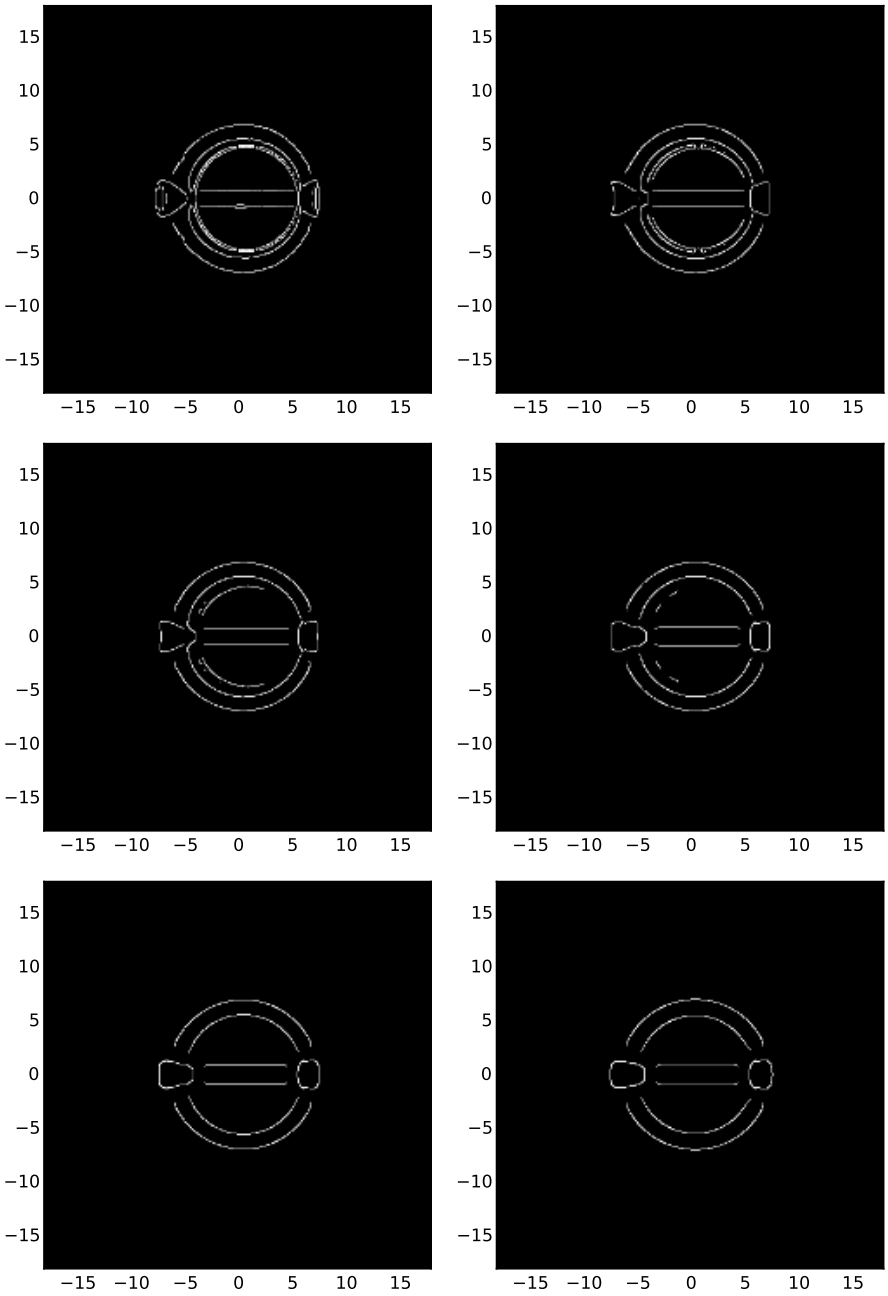

Figure 6.7: Edge detection by Canny's method for $\sigma = 1, 2, 3, 4, 5, 6$ (Left to right, top to bottom). The bigger the value for σ, the larger the size of the Gaussian filter becomes. This implies more blurring, necessary for noisy images, as well as detecting larger edges. As expected, however, the larger the scale of the Gaussian, the less accurate is the localization of the edge. Smaller values of σ imply a smaller Gaussian filter which limits the amount of blurring, maintaining finer edges in the image. (See Ref. [94] for further details)

6.2.0.2 Hough transform

In order to find a circle, a rough approximation of the shadow, in the image intensity, the information is converted into a binary edge-map, by a the gradient method described above and then the edge points vote to instantiate particular contour parameter values. For the circular limbic boundaries and a set of recovered edge points (x_i, y_i) for $j = 1, \ldots n$, a Hough transform is defined as [102, 94]

$$H\left(x_c, y_c, r\right) = \sum_{j=1}^{n} h\left(x_j, y_j, x_c, y_c, r\right) \tag{6.4}$$

where

$$h\left(x_j, y_j, x_c, y_c, r\right) = \begin{cases} 1 & if\ g\left(x_j, y_j, x_c, y_c, r\right) = 0 \\ 0 & otherwise \end{cases}$$

with

$$g\left(x_j, y_j, x_c, y_c, r\right) = \left(x_j - x_c\right)^2 + \left(y_j - y_c\right)^2 - r^2. \tag{6.5}$$

For each edge point (x_j, y_j), $g\left(x_j, y_j, x_c, y_c, r\right) = 0$ for every parameter triplet (x_c, y_c, r) that represents a circle through that point. Correspondingly, the parameter triplet that maximizes H is common to the largest number of edge points and is a reasonable choice to represent the contour of interest. In implementation, the maximizing parameter set is computed by building as an array that is indexed by discretized values for and . Once populated, the array is scanned for the triple that defines its largest value.

As an example, Fig. (6.8) shows the result of the Hough transformation applied to the bottom images of Fig. (5.4). where the Fig. (6.8, *Left*) has a circle of radius $54\,pixels$ drawn and Fig. (6.8, *Right*) a circle of radius $56\,pixels$ drawn.

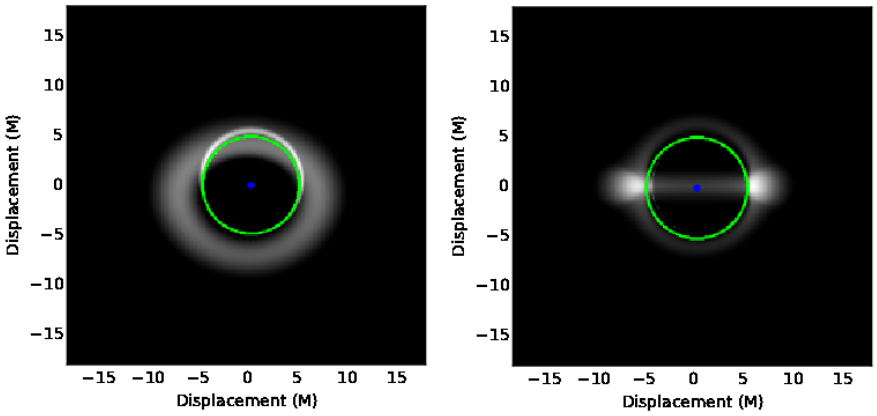

Figure 6.8: Illustrative results of shadow localization for Kerr black holes. See text for details.

Chapter 7

Discussion

Black holes are commonly believed to be the final states of the evolution of sufficiently massive stars, but their true nature is still far from clear. Within the following years, VLBI facilities will be able to directly image the accretion flow around Sgr A^*, our best black hole candidate. In particular, it will be possible to observe the black hole shadow –whose boundary corresponds to the apparent image of the photon capture sphere and is therefore determined by the spacetime geometry around the compact object– and image directly the accretion flow around it, opening a new window to test gravity in the strong field regime.

In this work, I have focused my attention on the "Kerrr" metric, a regular noncommutative inspired black hole. In order to explore the possibility of measuring this parameter from the shadow, images and spectra of Sgr A^*, I compared "Kerrr" to the Kerr solution. I have shown that, at least in principle, a very high precision measurement of the distortion parameters δ_s and ϵ breaks the degeneracy between the black hole spin and possible deviations from the Kerr geometry. Therefore, we can potentially test the Kerr metric via observations of its shadow. However, it is extremely difficult to distinguish between the Kerr case and the noncommutative case; if l_0 is large enough, the distortion parameters δ_s and ϵ will deviate by up to 4% of their value in the Kerr case.

The image and spectrum of Sgr A^*, as the case of study, was modeled using the relativistic ray-tracing code GYOTO, assuming an optically thin, constant angular momentum torus in hydrodynamic equilibrium around the Kerr and "Kerrr" geometries. The model used includes a toroidal magnetic field and radiative cooling by bremsstrahlung, synchrotron, and inverse Compton processes. It was shown that the black hole spin, torus dimensionless angular momentum and inclination each have a huge and and characteristic impact on the observed image and spectra of the torus, but the noncommutative parameter l_0 does not. It is challenging to test the Kerr metric of black hole candidates because most measurements cannot distinguish a Kerr black hole from a non-Kerr black hole with a different spin parameter, namely there is a degeneracy between the spin and possible deviations from the Kerr solution. In the case of Sgr A^*, in the near future it will be probably possible to have different measurements, which are sensitive to different relativistic effects, of the same object. If combined together, we can hope to be able to break the parameter degeneracy. The

assumptions provided here, for drawing the shadow and to model the accretion disk, do not provide a realistic scenario, but an easily accessible yet powerful analytical analogy.

Self-Disclosure:

- I have used geometrized units and, in the comparative cases, I chose the non-commutative parameter, to be almost-extremal. This gave me solutions with horizons that had the maximum allowed spin. However in these cases, the value is not physical, in the sense of the parameter's origin, i.e., *a minimal length* [90]. Nevertheless, it was conceptually interesting and lots of physics and computational techniques were developed in the process. The development of such analytic models and techniques are interesting as we wait for the Event Horizon Telescope data, where a large number of physical parameters will need to be explored. This work was done towards this direction.

- This work does not use the non-Gaussian smeared mass distributions considered in the article Phys. Lett. B Vol. 747: 564 (2015) by A. Larranaga, A. Cárdenas-Avendaño and D. Torres, which were first introduced in Adv. High Energy Physics, Vol 2013 (2013) by P. Nicolini, A. Orlandi and E. Spallucci. All the calculations presented here were derived and properly cited by myself.

References

[1] Abramowicz, M., Jaroszynski, M., and Sikora, M. Relativistic, accreting disks. *Astronomy and Astrophysics 63* (1978), 221–224.

[2] Abramowicz, M. A. Five ideas on black hole accretion disks. *ASP Conf.Ser. 403*, 29 (2009).

[3] Alvarez, E., and Conde, J. Are the string and einstein frames equivalent? *Modern Physics Letters A 17*, 07 (2002).

[4] Amarilla, L., and Eiroa, E. F. Shadow of a rotating braneworld black hole. *Phys. Rev. D 85*, 064019 (2012).

[5] Ansoldi, S. Spherical black holes with regular center. *arXiv 0802.0330* (2008).

[6] Ashtekar, A. The simplicity of black holes. *Physics 8*, 34 (2015).

[7] Atamurotov, F., A, A., and Ahmedov, B. Shadow of rotating horava lifshitz black hole. *Astrophys Space Sci 348* (2013), 179–188.

[8] Atamurotov, F., A, A., and Ahmedov, B. Shadow of rotating non-kerr black hole. *Phys. Rev. D 88*, 064004 (2013).

[9] Bambi, C. Testing the kerr black hole hypothesis. *Mod. Phys. Lett. A 26*, 2453 (2011).

[10] Bambi, C. A code to compute the emission of thin accretion disks in non-kerr spacetimes and test the nature of black hole candidates. *The Astrophysical Journal 761*, 174 (2012).

[11] Bambi, C. Testing the kerr nature of stellar-mass black hole candidates by combining the continuum-fitting method and the power estimate of transient ballistic jets. *Phys. Rev. D 85*, 043002 (2012).

[12] Bambi, C., Caravelli, F., and Modesto, L. Direct imaging rapidly-rotating non-kerr black holes. *Phys. Lett. B 711* (2012), 10–14.

[13] Bambi, C., Dolgov, A. D., and Petrov, A. A. Black holes as antimatter factories. *JCAP 0909*, 013 (2009).

[14] Bambi, C., Malafarina, D., and Tsukamoto, N. Note on the effect of a massive accretion disk in the measurements of black hole spins. *Phys. Rev. D 89*, 127302 (2014).

[15] Bardeen, J. M. Kerr metric black holes. *Nature 226* (1970), 64–65.

[16] Bardeen, J. M., Carter, B., Gursky, H., Hawking, S., Novikov, I., Ruffini, R., and Thorne, K. *Black Holes.* Gordon and Breach, Science Publishers, Inc., 1973.

[17] Bardeen, J. M., Press, W. H., and Teukolsky, S. A. Rotating black holes: Locally nonrotating frames, energy extraction, and scalar synchrotron radiation. *Astrophysical Journal 178* (1972), 347–370.

[18] Boyer, R. H., and Lindquist, R. W. Maximal analytic extension of the kerr metric. *Journal of Mathematical Physics 8*, 265 (1967).

[19] Broderick, A., Loeb, A., and Narayan, R. The event horizon of sagittarius a*. *Astrophysical Journal 701* (2009), 1357–1366.

[20] Broderick, A. E. Radiative transfer along rays in curved spacetimes. *MNARS 366*, L10-L12 (2006).

[21] Broderick, A. E., Johannsen, T., Loeb, A., and Psaltis, D. Testing the no-hair theorem with event horizon telescope observations of sagittarius a*. *The Astrophysical Journal 784*, 7 (2014).

[22] Camenzind, M. *Compact Objects in Astrophysics: White Dwarfs, Neutron Stars and Black Holes.* Springer-Verlag Berlin Heidelberg New York, 2007.

[23] Canny, J. F. Finding edges and lines in images. 720, Massachusets Inst. of Tech. Report, 1983.

[24] Cardenas-Avendano, A., and Larranaga, A. Probing spacetime regularity by measuring the shadow of a black hole. In *EHT Conference at the Perimeter Institute for Theoretical Physics* (2014).

[25] Carter, B. Global structure of the kerr family of gravitational fields. *Phys. Rev. 174* (1968), 1559.

[26] Carter, B. Axisymmetric black hole has only two degrees of freedom. *Phys. Rev. Lett. 26*, 6 (1971), 331–333.

[27] Chandrasekhar, S. *Radiative Transfer.* Dover Publications, 1960.

[28] Chandrasekhar, S. The kerr metric and stationary axisymmetric gravitational fields. *Proceedings of the Royal Society of London. Series A, Mathematical and Physical Sciences 358*, 1695 (1978).

[29] Chandrasekhar, S. *The Mathematical Theory of Black Holes.* Oxford Classic Texts in the Physical Sciences, Oxford University Press, USA, 1998.

[30] Cunningham, C. T. The effects of redshifts and focusing on the spectrum of an accretion disk around a kerr black hole. *Astrophys. J. 202* (1975), 788–802.

[31] Cunningham, C. T., and Bardeen, J. The optical appearence of a star orbiting an extereme kerr black hole. *The Astrophysical Journal 183* (1973), 237–264.

[32] Djorgovski, S. G., Volonteri, M., Springel, V., Bromm, V., and Meylan, G. The origins and the early evolution of quasars and supermassive black holes. *Proceedings of the MG11 Meeting on General Relativity* (2008), 340–367.

[33] Doeleman, S., Agol, E., Backer, D., Baganoff, F., Bower, G. C., Broderick, A., Fabian, A., Fish, V., Gammie, C., Ho, P., Honma, M., Krichbaum, T., Loeb, A., Marrone, D., Reid, M., Rogers, A., Shapiro, I., Strittmatter, P., Tilanus, R., Weintroub, J., Whitney, A., Wright, M., and Ziurys, L. Imaging an event horizon: submm-vlbi of a super massive black hole. *astro2010: The Astronomy and Astrophysics Decadal Survey 68* (2010).

[34] Doeleman, S. S., Weintroub, J., Rogers, A. E. E., Plambeck, R., Freund, R., Tilanus, R. P. J., Friberg, P., Ziurys, L. M., Moran, J. M., Corey, B., Young, K. H., Smythe, D. L., Titus, M., Marrone, D. P., Cappallo, R. J., Bock, D. C.-J., G. C. Bower, R. C., Davis, G. R., Krichbaum, T. P., Lamb, J., Maness, H., Niell, A. E., Roy, A., Strittmatter, P., Werthimer, D., Whitney, A. R., and Wood, D. Event-horizon-scale structure in the supermassive black hole candidate at the galactic centre. *Nature 455* (2008), 78–80.

[35] Douglas, M. R., and Nekrasov, N. A. Noncommutative field theory. *Reviews of Modern Physics 73*, 4 (2001).

[36] Drake, S. P., and Szekeres, P. Uniqueness of the newman janis algorithm in generating the kerr newman metric. *General Relativity and Gravitation 32*, 3 (2000), 445–457.

[37] Duda, and Hart. Use of the hough transformation to detect lines and curves in pictures. *Communications of the ACM 15*, 1 (1972), 11–15.

[38] Esin, A. A., Naryan, R., Ostriker, E., and Yi, I. Hot one-temperature accretion flows around black holes. *The Astrophysical Journal 465* (1996), 312–326.

[39] Falanga, M., Belloni, T., Casella, P., Gilfanov, M., Jonker, P., and King, A., Eds. *The Physics of Accretion onto Black Holes.* Springer, 2014.

[40] Falcke, H., and Markoff, S. The jet model for sgr a*: Radio and x-ray spectrum. *Astronomy and Astrophysics 362*, 113 (2000).

[41] Falcke, H., Melia, F., and Agol, E. Viewing the shadow of the black hole at the galactic center. *The Astrophysical Journal 528*, L13 L16 (2000).

[42] Fish, V. L., and Doeleman, S. S. Observing a black hole event horizon: (sub)millimeter vlbi of sgr a*. *IAU Symp 261* (2010).

[43] Gaensler, B. M., Haverkorn, M., Burkhart, B., Newton-McGee, K. J., Ekers, R. D., Lazarian, A., McClure-Griffiths, N. M., Robishaw, T., Dickey, J. M., and Green, A. J. Low-mach-number turbulence in interstellar gas revealed by radio polarization gradients. *Nature 478* (2011), 214–217.

[44] Ghez, A. M., Salim, S., Weinberg, N. N., Nu, J., Do, T., Dunn, J. K., Matthews, K., Morris, M. R., Yelda, S., Becklin, E. E., Kremenek, T., Milosavlijevic, M., and Naiman, J. Measuring distance and properties of the milky way's central supermassive black hole with stellar orbits. *The Astrophysical Journal 689*, 2 (2008).

[45] Grenzebach, A., Perlick, V., and Lammerzahl, C. Photon regions and shadows of kerr newman nut black holes with a cosmological constant. *Phys. Rev. D 89*, 12004 (2014).

[46] Gruppuso, A. Newton s law in an effective noncommutativ spacetime. *J. Phys. A Math. Gen. 38* (2005), 2039–2042.

[47] Hada, K., Doi, A., Kino, M., Nagai, H., Hagiwara, Y., and Kawaguchi, N. An origin of the radio jet in m87 at the location of the central black hole. *Nature 477* (2011), 185–187.

[48] Hada, K., Giroletti, M., Kino, M., Giovannini, G., D'Ammando, F., Cheung, C. C., Beilicke, M., Nagai, H., Doi, A., Akiyama, K., Honma, M., Niinuma, K., Casadio, C., Orienti, M., Krawczynski, H., Gomez, J. L., Sawada-Satoh, S., Koyama, S., Cesarini, A., Nakahara, S., and Gurwell, M. A. A strong radio brightening at the jet base of m 87 during the elevated very high energy gamma-ray state in 2012. *The Astrophysical Journal 788*, 2 (2014).

[49] Hansen, D., and Yunes, N. Applicability of the newman-janis algorithm to black hole solutions of modified gravity theories. *Phys. Rev. D 88*, 104020 (2013).

[50] Hansen, R. O. Multipole moments of stationary spacetimes. *Journal of Mathematical Physics 15*, 46 (1974).

[51] Hioki, K., and K-I, M. Measurement of the kerr spin parameter by observation of a compact object's shadow. *Phys. Rev. D 80*, 024042 (2009).

[52] Hough, P. V. C. Method and means for recognizing complex patterns. *U.S. Patent 3069654* (1962).

[53] Illingworth, J., and Kittler, J. A survey of the hough transform. *Comput. Vision, Graph. Image Processing 44* (1988), 87–116.

[54] James, O., von Tunzelmann, E., Franklin, P., and Thorne, K. Gravitational lensing by spinning black holes in astrophysics, and in the movie interstellar. *Class. Quantum Grav. 32*, 065001 (2015).

[55] Jaroszynski, M., Abramowicz, M. A., and Paczynski, B. Supercritical accretion disks around black holes. *Acta Astronomica 30*, 1 (1980), 1–34.

[56] Jiang, J., Bambi, C., and Steiner, J. Using iron line reverberation and spectroscopy to distinguish kerr and non kerr black holes. *Journal of Cosmology and Astroparticle Physics 1505*, 25 (2015).

[57] Johannsen, T. Photon rings around kerr and kerr like black holes. *The Astrophysical Journal 777*, 170 (2013).

[58] Johannsen, T., and Psaltis, D. Testing the no-hair theorem with observations in the electromagnetic spectrum. iv. relativistically broadened lines. *The Astrophysical Journal 773*, 57 (2013).

[59] Kalogera, V., and Baym, G. The maximum mass of a neutron star. *The Astrophysical Journal Letters 470*, 1 (1996).

[60] Kerr, R. P. Gravitational field of a spinning mass as an example of algebraically special metrics. *Phys. Rev. Lett. 11*, 237 (1963).

[61] Komissarov, S. S. Magnetized tori around kerr black holes: analytic solutions with a toroidal magnetic field. *Monthly Notices of the Royal Astronomical Society 368*, 993 (2006).

[62] Landau, L., and Liftshitz, E. *The Classical Theory of Fields.* Oxford, 1962.

[63] Li, Z., and Bambi, C. Destroying the event horizon of regular black holes. *Phys. Rev. D 87*, 124022 (2013).

[64] Li, Z., and Bambi, C. Measuring the kerr spin parameter of regular black holes from their shadow. *JCAP 1401:041* (2014).

[65] Luminet, J. Image of a spherical black hole with thin accretion disk. *Astronomy and Astrophysics 75*, 1-2 (1979).

[66] Mahadevan, R., Narayan, R., and Yi, I. Harmony in electrons: Cyclotron and synchrotron emission by thermal electrons in a magnetic field. *Astrophysical Journal 465* (1996), 327.

[67] Maier, D. *Black Hole Astrophysics: The Engine Paradigm.* Springer-Verlag Berlin Heidelberg, 2012.

[68] Melia, F. *High Energy Astrophysics.* Princeton University Press, 2009.

[69] Mihalas, D., and Mihalas, B. W. *Foundations of Radiation Hydrodynamics.* Oxford University Press, 1984.

[70] Modesto, L., and Nicolini, P. Charged rotating noncommutative black holes. *Phys. Rev. D. 82*, 10 (2010).

[71] Moffat, J. W. Modified gravity (mog) black holes and their observable shadows. *arXiv 1502.0677* (2015).

[72] Narayan, R., and Insu, I. Advection-dominated accretion: Underfed black holes and neutron stars. *Astrophysical Journal 452* (1995), 710.

[73] Nedkova, P. G., Tinchev, V. K., and Yazadjiev, S. S. Shadow of a rotating traversable wormhole. *Phys. Rev. D 88*, 12019 (2013).

[74] Newman, E. T., and Janis, A. I. Note on the kerr spinning particle metric. *J. Math. Phys. 6*, 915 (1965).

[75] Newman, E. T., and Penrose, R. An approach to gravitational radiation by a method of spin coefficients. *Journal of Mathematical Physics 3*, 3 (1962), 566 768.

[76] Nicolini, P. Noncommutative black holes, the final appeal to quantum gravity: A review. *International Journal of Modern Physics A 24*, 7 (2009), 1229–1308.

[77] Nicolini, P., Smailagic, A., and Spallucci, E. Noncommutative geometry inspired schwarzschild black hole. *Phys. Lett. B 632* (2006), 547.

[78] Pacholczyk, A. G. *Radio astrophysics. Nonthermal processes in galactic and extragalactic sources.* Series of Books in Astronomy and Astrophysics, San Francisco: Freeman, 1970.

[79] Papnoi, U., Atamurotov, F., Ghosh, S. G., and Ahmedov, B. Shadow of five-dimensional rotating myers perry black hole. *Phys. Rev. D 90*, 024073 (2014).

[80] Patnaik, S., and Yang, Y. M. *Soft Computing Techniques in Vision Science.* Springer, 2012.

[81] Price, R. H. Nonspherical perturbations of relativistic gravitational collapse. i. scalar and gravitational perturbations. *Phys. Rev. D 5*, 2419 (1972).

[82] Psaltis, D. Probes and tests of strong-field gravity with observations in the electromagnetic spectrum. *Living Rev. Relativity 11*, 9 (2008).

[83] Psaltis, D., Ozel, F., Chan, C.-K., and Marrone, D. P. A general relativistic null hypothesis test with event horizon telescope observations of the black-hole shadow in sgr a*. *arXiv 1411.1454* (2014).

[84] Psaltis, D., van der Klis, M., Strohmayer, T., Bildsten, L., McClintock, J., Remillard, R., Charles, P., Coe, M., Heise, J., in 't Zand, J., Kaspi, V., Roberts, M., Harding, A., Verbunt, F., Lewin, W., Fender, R., Kuulkers, E., Norton, A., Schwope, A., Warner, B., Kahabka, P., van den Heuvel, E., Fabbiano, G., White, N., King, A., Woods, P., Thompson, C., Hurley, K., Sari, R., Djorgovski, S., and Tauris, T. *Compact Stellar X-ray Sources*. Cambridge Univ. Press, 2010.

[85] Robinson, D. C. Uniquess of the kerr black hole. *Phys. Rev. Lett. 34*, 14 (1975), 905–906.

[86] Sakai, N., Saida, H., and Tamaki, T. Gravastar shadows. *Phys. Rev. D 90*, 104013 (2014).

[87] Smailagic, A., and Spallucci, E. Letter to the editor: Feynman path integral on the non-commutative plane. *Journal of Physics A: Mathematical and General 36*, 33 (2003).

[88] Smailagic, A., and Spallucci, E. Uv divergence-free qft on noncommutative plane. *Journal of Physics A: Mathematical and General 36*, 11545 (2003).

[89] Smailagic, A., and Spallucci, E. "kerr" black hole: The lord of the string. *Phys. Lett. B 688* (2010), 82.

[90] Snyder, H. S. Quantized space-time. *Phys. Rev. 71*, 38 (1947).

[91] Straub, O., Vincent, F. H., Abramowicz, M. A., Gourgoulhon, E., and Paumard, T. Modelling the black hole silhouette in sagittarius a* with ion tori. *A&A 543*, A83 (2010).

[92] Teukolsky, S. A. The kerr metric. *Class. Quantum Grav. 32*, 124006 (2015).

[93] Tsukamoto, N., Li, Z., and Bambi, C. Constraining the spin and the deformation parameters from the black hole shadow. *Journal of Cosmology and Astroparticle Physics 06*, 043 (2014).

[94] van der Walt, S., Schonberger, J. L., Nunez-Iglesias, J., Boulogne, F., Warner, J. D., Yager, N., Gouillart, E., Yu, T., and the scikit image contributors. scikit image: Image processing in python. *PeerJ Computer Science 2*, e453 (2014).

[95] Vazquez, S. E., and Esteban, E. P. Strong field gravitational lensing by a kerr black hole. *Nuovo Cim. B 119* (2004), 489–519.

[96] Vincent, F. H., Paumard, T., Gourgoulhon, E., and Perrin, G. Gyoto: a new general relativistic ray-tracing code. *Class. Quantum Grav. 28*, 225011 (2011).

[97] Vincent, F. H., Yan, W., Straub, O., Zdziarski, A. A., and Abramowicz, M. A. A magnetized torus for modeling sgr a* millimeter images and spectra. *Astronomy and Astrophysics 574*, A48 (2015).

[98] Visser, M. Physical observability of horizons. *Phys. Rev. D 90*, 127502 (2014).

[99] Walker, M., and Penrose, R. On quadratic first integrals of the geodesic equations for type [22] spacetimes. *Commun. Math. Phys. 18*, 265 (1970).

[100] Wei, S.-W., Cheng, P., Zhong, Y., and Zhou, X.-N. Probing spacetime noncommutative constant via black hole shadow. *arXiv 1501.06298* (2015).

[101] Wei, S. W., and Liu, Y. X. Observing the shadow of einstein-maxwell-dilaton-axion black hole. *Journal of Cosmology and Astroparticle Physics 11*, 063 (2013).

[102] Wildes, R. P. Iris recognition: An emerging biometric technology. *Proceedings of the IEEE 85*, 9 (1997).

[103] Wilkins, D. Bound geodesics in the kerr metric. *Phys. Rev. D 5*, 814 (1972).

[104] Will, C. M. The confrontation between general relativity and experiment. *Living Rev. Relativity 17*, 4 (2014).

[105] Yuan, F., and Narayan, R. Hot accretion flows around black holes. *Annual Reviews of Astronomy and Astrophysics 52* (2014), 529–588.

Appendix A

Derivation and Properties of the Kerr and "Kerrr" metrics

A.1 "Kerrr"

A.1.0.3 Noncommutative geometry

There is a long-held belief that alternative theories of gravity should have an uncertainty principle which prevents one from measuring positions to accuracies better than that given by the Planck length [76]: the momentum and energy required to make such a measurement would themselves modify the geometry at these scales. Therefore, one might wish to describe these effects, at least *effectively*, by a model theory having a new sort of uncertainty principle among the coordinates. Thus, and in analogy with coordinates and momenta in conventional quantum theory, the uncertainty would come from a noncommutative relation, postulating the existence of a noncommutative manifold [76]

$$[x^\mu, x^\nu] = i\theta^{\mu\nu}, \tag{A.1}$$

where $\theta^{\mu\nu}$ is an anti-symmetric matrix which determines the fundamental cell discretization of spacetime much in the same way as Planck constant $\hbar$ discretizes the phase space [77]. This idea was first proposed by Snyder in Ref. [90] as a way to improve the renormalizability properties of a theory at short distances or even to make it finite. However, this result was largely ignored due to the development of efficient renormalization techniques in field theories [76].

In Refs. [88, 87] was shown for the first time a model of quantum field theory on noncommutative spacetime, satisfying Lorentz invariance and unitarity, with no need for the Weyl–Wigner–Moyal-product [35] where the noncommutativity is carried by a Gaussian cut-off in the Fourier transform of the fields, which can be achieved assuming

$$\theta^{\mu\nu} = l_0^2 diag(\epsilon_{ij}, \epsilon_{ij}, \ldots),$$

where l_0 is a constant with dimension of length. This is not an *ad hoc* regularization

device but is a result coming from the averaging operation on coherent states [46].

It seems natural to modify the 4D Einstein action to incorporate noncommutative effects. However, as it was shown in Ref. [77], it is not necessary to change the Einstein tensor part of the field equations and the noncommutative effects can be implemented acting only on the matter source, since noncommutativity is considered an intrinsic property of the manifold itself, rather than a super-imposed geometrical structure and affects gravity in a subtle, indirect way. Hence, noncommutativity can be taken into account by keeping the standard form of the Einstein tensor in the l.h.s. of the field equations and introducing a modified energy–momentum tensor as a source in the r.h.s.

A.1.0.4 The static case

In a seminal work by Nicolini, Smailagic and Spallucci [77] was presented an inspired noncommutative Schwarzschild-like black hole based on Refs. [87, 88], where was explicitly shown that noncommutativity eliminates point-like structures in favor of smeared objects in flat space-time. In Ref. [77] the effect of smearing was mathematically implemented as a "substitution rule": position Dirac-delta function is replaced everywhere with a Gaussian distribution of minimal width l_0, a *minimal length,* which is reminiscent of the underlying noncommutativity of spacetime coordinates leading to the matter distribution [77], by choosing the mass density of a static, spherically symmetric, smeared, particle-like gravitational source as [77]

$$\rho_{l_o}(r) = \frac{M}{(4\pi\theta)^{\frac{3}{2}}} e^{\left(-\frac{r^2}{4l_o^2}\right)}, \tag{A.2}$$

which means that the total mass M is diffused throughout a region of linear size l_0. The mass enclosed in a volume of radius r is [89]

$$\begin{aligned} M \to M(r, l_0) &= 4\pi \int_0^r d\chi\, \chi^2 \rho_G(\chi) \\ &= \frac{M}{\Gamma\left(\frac{3}{2}\right)} \gamma\left(\frac{3}{2}; \left(\frac{r}{2l_0}\right)^2\right), \end{aligned} \tag{A.3}$$

$\gamma(b;\chi)$ is the lower incomplete gamma function[1]. Fig. (A.1) shows

The energy-momentum tensor was defined by considering the covariant conservation condition $T^{\mu\nu}_{\ ;\nu} = 0$ which, for a spherically symmetric metric is

$$\partial_r T^r{}_r = -\frac{1}{2} g^{00} \partial_r g_{00} \left(T^r{}_r - T^0{}_0\right) - g^{\theta\theta} \partial_r g_{\theta\theta} \left(T^r{}_r - T^\theta{}_\theta\right).$$

[1]The lower incomplete gamma function is defined as:

$$\gamma(b;x) \equiv \int_0^x \left(t^{b-1} e^{-t}\right) dt.$$

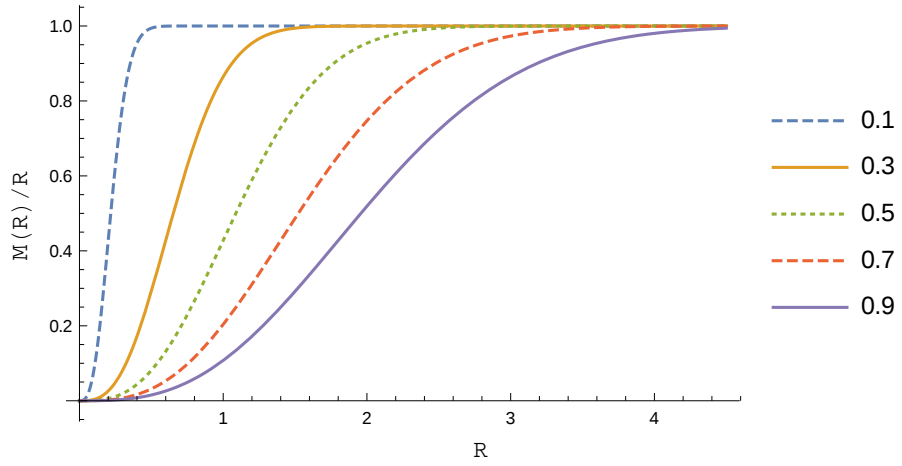

Figure A.1: Mass distribution for different values of the noncommutative parameter l_0. This figure can be compared with figure 1(a) of Ref. [100].

In order to preserve the Schwarzschild-like property $g_{00} = -g_{RR}^{-1}$, the condition $T^r{}_r = -T^0{}_0 = \rho_{l_0}(r)$ was imposed. Therefore, the divergence free equation allows a solution for $T^\theta{}_\theta$ which reads [77]

$$T^\theta{}_\theta = -\rho_{l_0}(R) - \frac{r}{2}\partial_R \rho(R).$$

Note that, rather than a massive structureless point, the source (A.2) turns out to be a self-gravitating droplet of anisotropic fluid of density ρ_{l_0}, radial pressure $p_r = -\rho_{l_0}$ and tangential pressure

$$p_\perp = -\rho_{l_0} - \frac{r}{2}\partial_r \rho_{l_0}.$$

The equations involving the energy-momentum tensor turn out to mean that there is a non-vanishing radial pressure balancing the inward gravitational pull and thus, preventing the collapse of the droplet into a matter point [76]. This is precisely the physical effect on matter caused by the existence of a fundamental length in spacetime and is the origin of all new physics at short distance scales.

Then the Einstein equations were solved[2]

$$G^\mu_\nu = R^\mu_\nu - \frac{1}{2} g^\mu_\nu R = 8\pi T^\mu_\nu,$$

with (A.2) as the matter source and using the line element

$$ds^2 = f(r)\, dt^2 - \frac{dr^2}{f(r)} - r^2\left(d\theta^2 + \sin^2\theta d\phi^2\right). \tag{A.4}$$

This gives the function[77]

[2]Here R is the Ricci scalar!

$$f(r) = 1 - \frac{M}{4\pi r \Gamma\left(\frac{3}{2}\right)} \gamma\left(\frac{3}{2}, \frac{r^2}{4l_0^2}\right). \tag{A.5}$$

The classical Schwarzschild metric is obtained from this solution in the limit $\frac{r}{l_0} \to \infty$. In Ref. [77] was studied the horizon(s) structure, thermodynamics and regularity of the solution (A.4) and in Ref. [5] can be found a comprehensive study of the geometrical properties of the solution (A.4) and a discussion on the energy conditions.

A.1.0.5 The rotating case

The Newman-Janis algorithm [74] is a short cut to obtain spinning black hole solutions from the corresponding non rotating ones and it has been shown that it works for vacuum solutions or for solutions with a Maxwell source [36]. The black hole solution (A.4) is not a vacuum solution, since Einstein equations have an anisotropic fluid as source, and therefore the application of the Newman-Janis procedure is not straightforward but in Ref. [70] Modesto and Nicolini provided a modification to include non vanishing stress-energy tensors and, using this modification of the algorithm and the five steps presented in Ref. [36], the rotating black holes based on the smeared mass distribution (A.2) is found [3].

To start, the line element (A.4) must be changed to the outgoing Eddington-Finkelstein coordinates $\{u, R, \vartheta, \phi\}$, where $u = t - R^*$and $dR^* = \frac{dR}{f(R)}$, to obtain the metric

$$ds^2 = f(R)\, du^2 + 2 du dR - R^2\left(d\theta^2 + \sin^2\theta d\phi^2\right). \tag{A.6}$$

This metric can be written in terms of null tetrad vectors as [75]

$$g_{\mu\nu} = l_\mu n_\nu + l_\nu n_\mu - k_\mu \bar{k}_\nu - k_\nu \bar{k}_\mu,$$

where the tetrad vectors are

$$\begin{aligned} l^\mu &= \delta^\mu_1, \\ n^\mu &= \delta^\mu_0 - \frac{1}{2} f(R)\, \delta^\mu_1, \\ k^\mu &= \frac{1}{\sqrt{2R^2}}\left[\delta^\mu_2 + \frac{i}{\sin\theta}\delta^\mu_3\right], \end{aligned}$$

satisfying the relations $l_\mu l^\mu = k_\mu k^\mu = n_\mu n^\mu = l_\mu k^\mu = n_\mu k^\mu = 0$ and $l_\mu n^\mu = -k_\mu \bar{k}^\mu = 1$, with $\bar{k}$ being the complex conjugate of k. The following step in the Newman-Janis algorithm is to perform the complex increment

[3] In Ref. [49] was found that the application of the Newman-Janis algorithm to an arbitrary non-GR spherically symmetric solution introduces pathologies in the resulting axially symmetric metric, establishing that, in general, the Newman-Janis algorithm should not be used to construct rotating black hole solutions outside of General Relativity. However, as has been seen here, General Relativity has not been changed at all, just an anisotropic fluid as source was included.

$$\begin{cases} R & \to R' = R + ia\cos\theta \\ u & \to u' = u - ia\cos\theta, \end{cases} \tag{A.7}$$

which is the key point of the algorithm. In the limiting case $l_0 \to 0$, the metric $(A.4)$ coincides with the Schwarzschild solution, i.e., the mass function becomes $m(R) = M$, and the usual algorithm can be followed [70].

The mass term is unaffected by the complexification $(A.7)$ and it is assumed that [36]

$$\frac{1}{R} \mapsto \frac{1}{2}\left(\frac{1}{R'} + \frac{1}{\bar{R}'}\right) = \frac{R}{R^2 + a^2\cos^2\theta}.$$

Therefore, the proposal for the complexification of the function $f(R)$ given in equation $(A.5)$ is to make $m(R) \to m[\mathrm{Re}(R')] = m(R)$ which gives

$$\begin{aligned} f(R) &= 1 - \frac{2m(R)}{R} \\ &\to 1 - 2m[\mathrm{Re}(R')]\left[\frac{1}{2}\left(\frac{1}{R'} + \frac{1}{\bar{R}'}\right)\right] \\ &= 1 - \frac{2m(R)R}{R^2 + a^2\cos^2\theta} = F(R,\theta), \end{aligned}$$

or writing the obtained function in terms of the gamma functions,

$$F(R,\theta) = 1 - \frac{M}{4\pi\Gamma\left(\frac{3}{2}\right)}\frac{R}{R^2 + a^2\cos^2\theta}\gamma\left(\frac{3}{2}, \frac{R^2}{4l_0^2}\right).$$

Thus, the tetrad vectors are

$$\begin{aligned} l^\mu &= \delta_1^\mu, \\ n^\mu &= \delta_0^\mu - \frac{1}{2}F(R,\theta)\,\delta_1^\mu \end{aligned}$$

and

$$k^\mu = \frac{1}{\sqrt{2\left(R^2 + a^2\cos^2\theta\right)}}\left[ia\sin\theta\left(\delta_0^\mu - \delta_1^\mu\right) + \delta_2^\mu + \frac{i}{\sin\theta}\delta_3^\mu\right],$$

from which the metric of the rotating regular black hole can be cast in Boyer-Lindquist coordinates,

$$
\begin{aligned}
ds^2 &= F(R,\theta)\,dt^2 - \frac{\Sigma dR^2}{a^2\sin^2\theta + F(R,\theta)\,\rho^2} \\
&\quad +2\left(1-F(R,\theta)\right)a\sin^2\theta dt d\phi - \rho^2 d\theta^2 \\
&\quad -\left[a^2\left(2-F(R,\theta)\right)\sin^2\theta + \rho^2\right]\sin^2\theta d\phi^2,
\end{aligned}
$$

where

$$
\rho^2 = R^2 + a^2\cos^2\theta.
$$

By introducing the quantity

$$
\Delta = \rho^2 F(R,\theta) + a^2\sin^2\theta = R^2 - 2Rm(R) + a^2,
$$

the latter metric can be written in the usual form

$$
\begin{aligned}
ds^2 &= \frac{\Delta - a^2\sin^2\theta}{\rho^2}dt^2 - \frac{\rho^2 dR^2}{\Delta} - \rho^2 d\theta^2 \\
&\quad -\left[\rho^2 + a^2\sin^2\theta\left(2 - \frac{\Delta - a^2\sin^2\theta}{\rho^2}\right)\right]\sin^2\theta d\phi^2 \\
&\quad +2a\sin^2\theta\left(1 - \frac{\Delta - a^2\sin^2\theta}{\rho^2}\right)dt d\phi, \qquad \text{(A.8)}
\end{aligned}
$$

which is exactly the rotating noncommutative inspired black hole shown by Smailagic and Spallucci in Ref. [89] but there was derived in a more "physical" way, by exploiting the common properties of Schwarzschild and Kerr solutions.

A.1.0.6 Properties

As has been seen above, this kind of solution can be achieved by "simply" substituting the mass function into the mass term of Schwarzschild and Kerrr metrics, respectively. Therefore the classical Schwarzschild and Kerr metrics are obtained from this solution in the limit $\frac{R}{l_0} \to \infty$ [77].

Here, I this work I have used R instead of r mainly for two reasons, the first is to distinguish it easily from the geometry presented in Chap. 2 and the second is to clarify the coordinates used to described an axially symmetric spheroidal geometry as was done in Ref. [89], i.e.,

$$
\begin{aligned}
x &= \sqrt{R^2 + a^2}\sin\theta\cos\phi \\
y &= \sqrt{R^2 + a^2}\sin\theta\sin\phi \\
z &= R\cos\theta,
\end{aligned}
$$

in which surfaces described by these coordinates are cofocal ellipsoids, for $R =$

constant, and cofocal hyperboloids, for $\theta = const$, with foci on the ring

$$(0, a\cos\phi, a\sin\phi, 0)\,.$$

These surfaces are described by $\pi/2$

$$\frac{x^2+y^2}{R^2+a^2} + \frac{z^2}{R^2} = 1,$$

$$\frac{x^2+y^2}{a^2\sin^2\theta} - \frac{z^2}{a^2\cos^2\theta} = 1,$$

and by taking $y = 0$, for simplicity, the asymptote of the hyperbola is

$$z = x\cot\theta.$$

Thus, θ is the angle between the z-axis and the asymptote of the hyperbola and R is the smaller semi-axis of the ellipse. Any function $f(R)$ is not to be considered a radial function in the usual sense [89]. It can be shown that the Ricci $R_{(rot)}$ and Kretschmann $K_{(rot)}$ scalars, are regular in the point $R = 0$, $\theta = \frac{\pi}{2}$, but discontinuous (they assume two different values depending of the way one reaches that point, as in Ref. [70]), and this is the reason why this solutions are considered "r"egulars.

A.2 Kerr

The classical Kerr metric can be recovered from (A.8) in the limit $R/l_0 \to \infty$. However, there are more physical ways to obtain it and here I just want to make a few remarks about its derivation.

Landau and Liftshitz said in 1962 that [62]:

> "*There is no constructive analytic derivation of the Kerr metric that is adequate in its physical ideas, and even a check of this solution of Einstein's equations involves cumbertone calculations*".

Sixteen years later, in 1978, Chandrasekhar said that [28]:

> "*...it is striking that there is no extant derivation of Kerr's solution that is direct and simple*"

and in Ref. [29] it was first derived and properly reduced the equations leading to the Kerr metric. Nevertheless, the situation has not changed over the past years, even today its derivation from some reasonable assumptions is still not easy [92]. The Kerr metric can be derived in a systematic way as is done in Refs. [28] and [22].

Appendix B

Poster Presented at the EHT 2014

[Perimeter Institute for Theoretical Physics]